





REVIEW ARTICLE | APRIL 18 2024

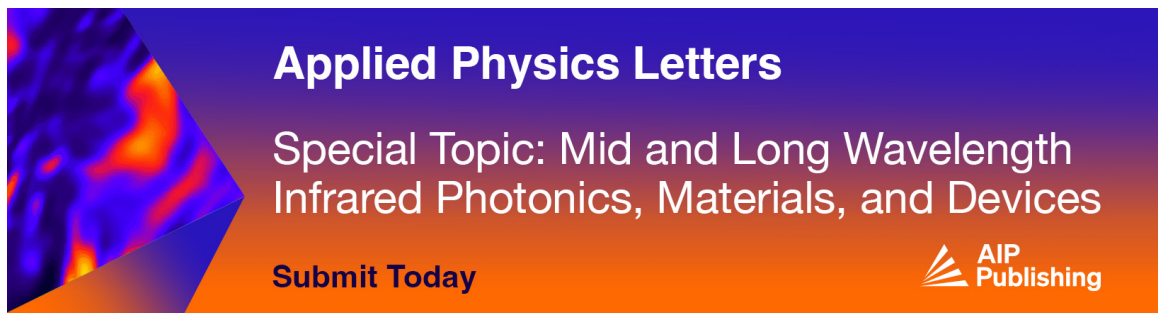
## Coupled mode theory for plasmonic couplers

Alessandro Tuniz ; Alex Y. Song ; Giuseppe Della Valle ; C. Martijn de Sterke 



*Appl. Phys. Rev.* 11, 021309 (2024)


<https://doi.org/10.1063/5.0182361>



**Applied Physics Letters**

Special Topic: Mid and Long Wavelength Infrared Photonics, Materials, and Devices

**Submit Today**



# Coupled mode theory for plasmonic couplers

Cite as: Appl. Phys. Rev. **11**, 021309 (2024); doi: [10.1063/5.0182361](https://doi.org/10.1063/5.0182361)

Submitted: 18 October 2023 · Accepted: 14 March 2024 ·

Published Online: 18 April 2024



View Online



Export Citation



CrossMark

Alessandro Tuniz,<sup>1,2,a)</sup>  Alex Y. Song,<sup>3</sup>  Giuseppe Della Valle,<sup>4</sup>  and C. Martijn de Sterke<sup>1,2</sup> 

## AFFILIATIONS

<sup>1</sup>Institute of Photonics and Optical Science (IPOS), School of Physics, The University of Sydney, NSW 2006, Australia

<sup>2</sup>The University of Sydney Nano Institute, The University of Sydney, NSW 2006, Australia

<sup>3</sup>School of Electrical and Information Engineering, The University of Sydney, NSW 2006, Australia

<sup>4</sup>Dipartimento di Fisica, Politecnico di Milano, P.zza Leonardo da Vinci 32, Milan 20133, Italy

<sup>a)</sup>Author to whom correspondence should be addressed: [alessandro.tuniz@sydney.edu.au](mailto:alessandro.tuniz@sydney.edu.au)

## ABSTRACT

Photonic integrated circuits play an increasingly important role in several emerging technologies. Their functionality arises from a combination of integrated components, e.g., couplers, splitters, polarization rotators, and wavelength selective filters. Efficient and accurate simulation of these components is crucial for circuit design and optimization. In dielectric systems, design procedures typically rely on coupled-mode theory (CMT) methods, which then guide subsequent refined full-wave calculations. Miniaturization to deep sub-wavelength scales requires the inclusion of lossy plasmonic (metal) components, making optimization more complicated by the interplay between coupling and absorption. Even though CMT is well developed, there is no consensus as to how to rigorously and quantitatively implement it for lossy systems. Here we present an intuitive coupled-mode theory framework for quantitative analysis of dielectric-plasmonic directional and adiabatic couplers, whose large-scale implementation in 3D is prohibitively slow with full-wave methods. This framework relies on adapting existing coupled mode theory approaches by including loss as a perturbation. This approach will be useful in designing dielectric-plasmonic circuits, providing a first reference point for anyone using techniques such as inverse design and deep learning optimization methods.

Published under an exclusive license by AIP Publishing. <https://doi.org/10.1063/5.0182361>

## TABLE OF CONTENTS

I. INTRODUCTION.....	1	VII. ADIABATIC COUPLER.....	14
II. HISTORICAL OVERVIEW.....	3	VIII. APPLICATION TO 3D WAVEGUIDES.....	16
III. THEORY.....	3	A. Chip-based plasmonic coupler.....	16
A. Coupled mode picture.....	3	1. Directional coupler.....	16
B. Eigenmode picture.....	4	2. Adiabatic coupler.....	17
IV. THE COUPLED MODE PARAMETERS.....	5	B. Fiber-based plasmonic coupler.....	18
A. Perturbative approach.....	5	1. Directional coupler.....	19
B. Exact CMT approach (CMT <sub>e</sub> ).....	6	2. Adiabatic coupler.....	19
C. Simplified CMT approach (CMT <sub>s</sub> ).....	6	IX. COMPARISON WITH EXPERIMENTS.....	19
D. Lossless case.....	6	X. COMPUTATIONAL RESOURCE COMPARISON.....	20
E. Lossy case.....	7	XI. CONCLUSION.....	21
V. EXPRESSION FOR THE POWER IN EACH MODE.....	8		
A. Coupled mode theory approaches.....	8	I. INTRODUCTION	
B. Eigenmode approaches.....	9	Photonic integrated circuits (PICs) and related technologies are rapidly moving from proof-of-concept prototypes to consumer products, driven by telecommunications, <sup>1</sup> quantum, <sup>5</sup> smart, <sup>3,4</sup> and sensing <sup>5</sup> applications, complemented by the growing number of accessible photonic manufacturing foundries. PICs support many different materials, e.g., including silicon, <sup>6</sup> lithium niobate, <sup>7</sup> glasses, <sup>8</sup> nitrides, <sup>9</sup> polymers, <sup>10</sup> and III-V semiconductors, <sup>11</sup> and hybrid configurations thereof. <sup>12</sup> Each	
VI. DIRECTIONAL COUPLING.....	10		
A. An explorer's map.....	12		
B. Wavelength dependence.....	12		
C. Plasmonic sensing.....	13		
D. The exceptional point.....	14		

have their own particular set of advantages and disadvantages, but are nevertheless starting to appear in commercially available products.<sup>6</sup>

Typical PICs rely on the guidance of light inside a high-index dielectric waveguide, where the degree of lateral confinement is typically on the order of 200 nm at NIR wavelengths due to diffraction, which thereby imposes a fundamental limit on minimum footprint of each individual PIC building block. Further miniaturization can only be achieved using metals which support surface plasmon polaritons,<sup>13</sup> which can give rise to lateral confinement down to the few-nanometer scale.<sup>14</sup> The resulting sub-wavelength confinement is not achievable with dielectric waveguides and enables ultra-compact photonic devices with significantly enhanced field intensities resulting in strong light-matter interactions. The integration of such plasmonic elements into PICs is also being pursued both fundamentally<sup>15</sup> and commercially,<sup>16</sup> with the value proposition that they can operate at a lower power and smaller footprint to achieve large optical nonlinearities<sup>17</sup> and can interface with ultrafast electronics.<sup>18</sup> One of the fundamental problems with plasmonic waveguides, however, is the large mode losses per unit wavelength—orders of magnitude larger than their all-dielectric counterparts.<sup>13</sup> Because fields can be enhanced by many orders of magnitude, long waveguides are often not needed, and losses can be managed with appropriate device designs.

One of the most important elements in PICs is the photonic coupler, whose role is to transfer light between adjacent waveguides via evanescent coupling, relying on accurate models in order to design the correct waveguide dimensions. One of the earliest and most important stages of the PIC circuit design flow<sup>6</sup> is circuit simulation, which is typically performed by calculating propagation through the geometry via finite difference time domain (FDTD),<sup>19</sup> eigenmode expansion (EM expansion),<sup>20</sup> finite element method (FEM),<sup>21</sup> or beam-propagation method (BPM).<sup>22</sup> Although these remain the preferred methods when refining a specific geometry, one oft-overlooked method that underpins the available parameter space from the outset, and which describes photonic couplers in their most fundamental form, is coupled mode theory (CMT),<sup>23</sup> which forms the focus of this work.

In the context of PIC design, several issues make the integration of plasmonic elements challenging using any of the above methods. First, metallic losses imply that trade-offs between coupling lengths and absorption lengths need to be appropriately accounted for: while all-dielectric PICs can support centimeters of propagation and incur only modest losses, plasmonic couplers must be kept to as short as

possible because losses can hinder coupler performance before any power transfer occurs. Furthermore, plasmonic models using full-wave methods typically require a fine mesh—of the order of a fraction of the nanoscale mode volume—making full 3D simulations computationally demanding. Although coupled mode theory can, in principle, provide fundamental insight, there is no generally accepted procedure as to how it should be implemented.

Here, we present a simplified coupled mode theory model (CMT<sub>s</sub>), which considers plasmonic couplers in the simplest and most abstract form. Our model assumes that dielectric–plasmonic coupling is a perturbation to the lossless case,<sup>24</sup> and enables us to construct an “explorer’s map” of the maximum coupling efficiency and its associated optimal device length as a function of modal parameters. This map will likely be useful in the first design steps of any dielectric–plasmonic PIC. As we will show, this abstract model is widely applicable to several realistic designs, including resource-intensive 3D couplers, whose embodiment can take many different forms. Figure 1 shows a non-exhaustive schematic summary of the plasmonic–dielectric couplers that could benefit from our formalism. The device function is summarized in Fig. 1(a), which shows a dielectric waveguide (blue) adjacent to a lossy nano-plasmonic waveguide (yellow), so that the fundamental mode of a dielectric waveguide couples to the plasmonic mode. Because CMT is agnostic to the underlying waveguides that support the modes, our approach can be applied to a variety of waveguide systems that include (but are not limited to) nanowires,<sup>25,26</sup> gap plasmonic systems,<sup>27</sup> hybrid plasmonic waveguides,<sup>28</sup> and cylindrical waveguides<sup>29</sup> (e.g., for fiber-based plasmonic applications<sup>30</sup>), each shown in Fig. 1(b).

The remainder of the paper is structured as follows. Section II is a historical overview of coupled mode theory, including lossless and lossy implementations. Section III presents the fundamental theory underpinning coupled mode theory and eigenmode theory, as well as the simplified coupled mode theory for plasmonic waveguides. Section IV reviews the methods for calculating coupled mode parameters, using exact and perturbative approaches. Section V provides an overview on the various expressions which can be used for calculating the power in each waveguide. Sections VI and VII quantitatively present each methods’ accuracy, using 2D directional and adiabatic couplers, discussing the practical limits of the simplified CMT theory. This, in turn, allows us to present a map of the minimum transfer length and maximum transfer power for any plasmonic directional coupler as a

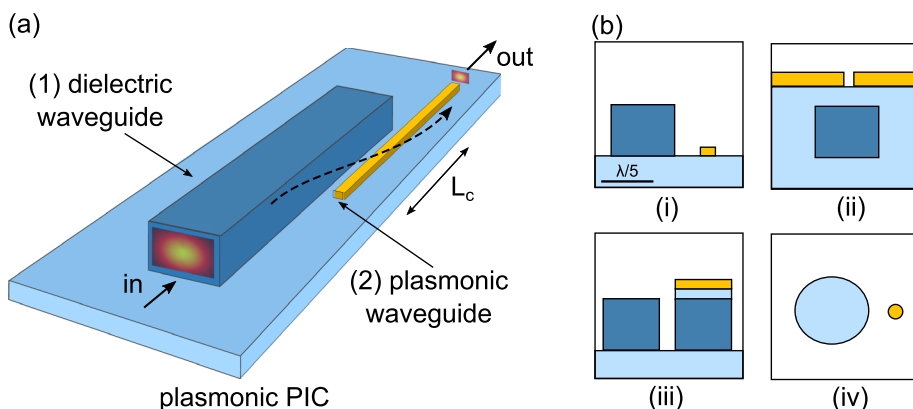


**FIG. 1.** (a) Concept schematic of the present study. A photonic-plasmonic coupler, forming the compact building block of a PIC, is formed by a wavelength-scale dielectric waveguide (dark blue) adjacent to a plasmonic element (yellow) of sub-wavelength transverse dimensions. Light is injected into the dielectric waveguide, and ideally efficiently couples into the plasmonic element, which provides subwavelength guidance at output. (b) The formalism presented can be readily applied to a family of structures which includes (i) planar nanowires, (ii) gap plasmonic systems, (iii) hybrid plasmonic waveguides, and (iv) cylindrical waveguides.

function of modal parameters. In Sec. VIII, we discuss how our method applies to realistic 3D waveguides, including planar and fiber structures. Then in Sec. IX, we compare the results of our method to a recent set of experiments, whereas in Sec. X we compare the required computational resources of our method to that of conventional methods. We then conclude in Sec. XI.

## II. HISTORICAL OVERVIEW

Coupled-mode theory has a long and rich history, and continues to be widely employed. It is often used as a first pedagogical introduction to waveguide coupling, due to its ability to intuitively elucidate the physics and accurately predict the performance of practical devices with minimal computational effort, and which distinguishes it from computationally intensive full-wave numerical simulations. In turn, CMT can be broadly classified into two types: the coupling of modes in time, a.k.a. temporal coupled mode theory, and the coupling of modes in space, a.k.a. spatial coupled mode theory.

Temporal CMT holds broad applicability across various wave phenomena such as electromagnetics, resonating modes in electronic circuits, and mechanical waves. It deals with the evolution of a system in time, where the system typically comprises several resonator modes possibly with input and output channels. A pedagogical introduction to temporal CMT can be found in a number of references such as Ref. 31. For a rigorous exposition of temporal CMT for generic multi-mode multi-channel optical systems featuring nonorthogonal modes, please refer to Ref. 32.

In contrast, spatial CMT addresses the evolution of waves in space, typically along coupled waveguide systems. As we will show in Sec. III, a typical form of CMT equations for two waveguide modes can be written as follows:

$$\begin{aligned} -i \frac{d}{dz} \psi_1 &= \gamma_1 \psi_1 + \kappa_{12} \psi_2 \\ -i \frac{d}{dz} \psi_2 &= \gamma_2 \psi_2 + \kappa_{21} \psi_1, \end{aligned} \quad (1)$$

where indices 1 and 2 can represent two parallel waveguides separated by a finite distance, and  $\psi_1$  and  $\psi_2$  are  $z$ -dependent amplitudes that multiply the stand-alone eigenmodes of each waveguide. Here,  $\gamma_{1,2}$  are the propagation constants of these two modes, and  $\kappa_{12}$  and  $\kappa_{21}$  are their coupling constants. Each waveguide may support multiple modes, which form a complete basis, yet in many cases the high-order modes are ignored as an approximation.  $\kappa_{12}$  and  $\kappa_{21}$  can be intuitively understood as the evanescent coupling between the modes. The simplest form of the coupling constants can be written as<sup>31</sup>

$$\kappa_{12} = \frac{\omega}{4} \int \delta\epsilon \vec{E}_1^* \cdot \vec{E}_2 dx, \quad (2)$$

where  $\omega$  is the wave frequency, and  $E_1$  and  $E_2$  are the electric field distributions of the two eigenmodes, each in one standalone waveguide, respectively. Here,  $\delta\epsilon(x)$  is a change in the permittivity in space by introducing waveguide 1 to the space where originally only waveguide 2 exists, and  $\kappa_{21}$  can be defined similarly. Although (2) can be rigorously derived from a variational principle,<sup>31</sup> it can also be intuitively interpreted as a perturbation, i.e.,  $-i\omega\delta\epsilon E_1$  is the extra polarization current generated by mode 1 with the introduction of waveguide 1, so that the coupling parameter  $\kappa_{12}$  is simply the transfer of energy from this current to mode 2. However, such a simple expression only gives

correct results when the propagation constants of the two modes are identical – in more rigorous formulations the definitions of  $\gamma_1$ ,  $\gamma_2$ ,  $\kappa_{12}$ , and  $\kappa_{21}$  become more complicated, as we will discuss in Sec. III.

Spatial CMT emerged in the broad context of waveguides in the 1950s,<sup>33,34</sup> and was later adapted to optical waveguides (e.g., optical fibers) in the 1970s.<sup>35–38</sup> Early spatial CMT approaches relied on heuristic and physically intuitive pictures, and were often derived by inspection. Over the years, significant efforts were dedicated toward enhancing the rigor and accuracy of spatial CMT, such as a derivation based on the variational principle,<sup>31</sup> expansion onto known complete bases,<sup>39</sup> formulations based on nonorthogonal modes in the 1980s,<sup>40–44</sup> and a derivation starting from reciprocity.<sup>45</sup> Interested readers are directed to Sec. II of Ref. 23 for a detailed historical perspective of spatial CMT, in conjunction with other reviews and books.<sup>31,46–50</sup> It is worth noting that the term “spatial CMT” is also commonly used in other scenarios involving the coupling of two modes due to a perturbation in the permittivity. This context often involves overlap integrals of the type Eq. (2), where  $E_{1,2}$  represents modes of an unperturbed system, and  $\delta\epsilon$  represents a perturbation in space. These two modes can be waveguide modes, resonator modes, or any unguided modes. However, such calculations are, in general, mathematically rigorous only to first order.<sup>51</sup> The scope of these applications of spatial CMT is beyond the focus of the current paper.

Following the above developments, spatial CMT can yield accurate results for coupled waveguides with a large separation, i.e., in a weakly coupled scenario. Nevertheless, in recent years, spatial CMT has been applied to new structures featuring closely spaced dielectric and plasmonic waveguides, albeit without comprehensive validation. However, in such a strongly coupled scenario, previous formulations of spatial CMT, which do not involve calculations of the true eigenmodes of the actual coupled waveguides, fail to provide precise results. This is understandable, as the proximity of the waveguides transcends the realm of perturbation and the removal of high-order modes from the complete basis is an unregulated approximation. This can be effectively addressed through the utilization of the true eigenmodes of the whole coupled system, as initially presented in Appendix F of Ref. 42. Yet, this formulation still entails cumbersome spatial overlap integrals. To the best of our knowledge, this formulation has not gained widespread adoption.

We will turn our attention to reviewing the aforementioned spatial CMT formulations in the context of dielectric–plasmonic couplers, leading into a simplified and streamlined CMT formulation utilizing the true eigenmodes of the actual coupled waveguide system, showing that the simplified method yields remarkably accurate predictions, even for waveguides that are quite strongly coupled. This approach is motivated by recent developments in numerical algorithms and computing hardware, where solving for the eigenmodes in 2D, i.e., the modal profiles in the cross section of coupled waveguides, poses almost no significant challenge.

## III. THEORY

### A. Coupled mode picture

Waveguides such as those shown schematically in Fig. 1 are described by several parameters (refractive indices and dimensions of each waveguide, spacing of the waveguides, refractive index of the region between and outside the waveguides), all of which are most generally functions of propagation length. To help guide the reader, we ground our discussion using the particular one-dimensional slab device

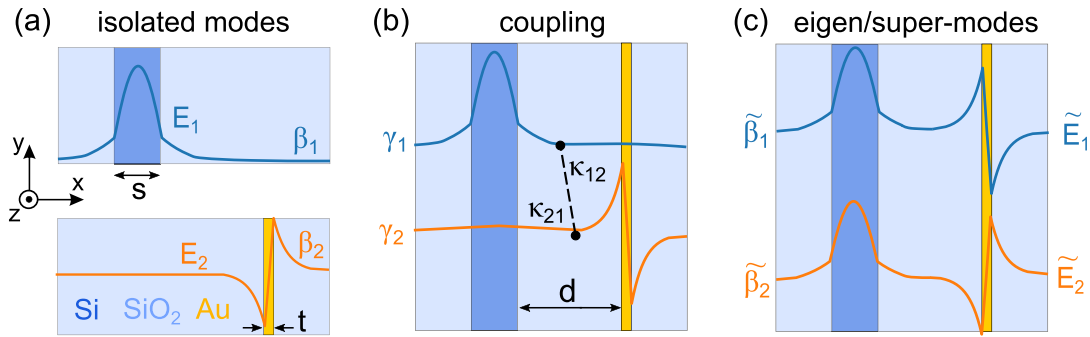


**FIG. 2.** Schematic summary of different physical pictures, modes, and parameters used for calculating the power exchanged by dielectric and plasmonic waveguides, using 1D waveguides (infinite in  $y$ ) with propagation along the  $z$  axis as an illustrative example. (a) The isolated modes are formed either by a dielectric waveguide of width  $s$  or a metal film of thickness  $t$  surrounded by a low-index material. These waveguides support modes with propagation constants  $\beta_i$  and electric field profiles  $E_i$ . (b) When the waveguides are brought together separated by a distance  $d$ , they couple via  $\kappa_{ij}$ , and their respective propagation constant is  $\gamma_i$  because of the neighboring waveguide. (c) The two-waveguide system supports supermodes with propagation constants  $\tilde{\beta}_i$  and electric field profiles  $\tilde{E}_i$ .

shown in Fig. 2, and which constitutes our leitmotif for the first half of this work. Fig. 2(a) shows the individual waveguides. We take the dielectric waveguide (dark blue) to be a silicon slab (width:  $d = 220$  nm, refractive index: 3.5); the metal waveguide (yellow) is taken to be a gold thin film (thickness:  $t = 7.5$  nm), and its permittivity is given by a Drude model.<sup>52</sup> The waveguide width and metal thickness are taken to be  $z$ -independent for now. The background is silica.<sup>53</sup> Figure 2(b) shows the coupled waveguides, which are separated by a distance  $d$ . In first instance and for illustrative purposes, we assume the gold to be lossless (i.e., its permittivity is taken to be the real part of its actual value<sup>52</sup>); we discuss the effect of losses in detail, starting in Sec. IV.

We take each individual waveguide to support only one guided mode, so that the total transverse electric and magnetic fields of the coupled system are, respectively,

$$\mathbf{E}(x, y, z) = \psi_1(z)\mathbf{E}_1(x, y) + \psi_2(z)\mathbf{E}_2(x, y), \quad (3)$$

$$\mathbf{H}(x, y, z) = \psi_1(z)\mathbf{H}_1(x, y) + \psi_2(z)\mathbf{H}_2(x, y), \quad (4)$$

where we have neglected the residual fields<sup>42</sup> for simplicity. Modes are normalized such that  $C_{11} = C_{22} = 1$ , where

$$C_{ij} = \hat{z} \cdot \iint \frac{1}{2} [\mathbf{E}_j \times \mathbf{H}_i] dx dy. \quad (5)$$

With this definition,  $\psi_i$  is the mode amplitude defined such that  $|\psi_i|^2$  corresponds to the normalized power carried by the mode (provided that the mode is lossless, as discussed in Sec. V).

We start by considering each individual guide separately, corresponding to the case where the two waveguides are infinitely far apart, and illustrated schematically in Fig. 2(a). In this case, each waveguide's  $z$ -dependent amplitude is  $\psi_i(z) = \exp(i\beta_i z)$ . The propagation in a uniform, isolated waveguide  $i$  is thus described by  $-id\psi_i/dz = \beta_i\psi_i$ . For the isolated waveguides, the index “1” and “2” refer to the dielectric and plasmonic modes, respectively. The dashed lines in Fig. 3(a) show the effective index  $\beta_i/k_0$  as a function of wavelength for each mode and our choice of parameters, where  $k_0 = 2\pi/\lambda$ . Our choice of parameters is such that the two waveguides are phase-matched at  $\lambda = 1.55$   $\mu\text{m}$  (i.e.,  $\beta_1 = \beta_2$ ).

When the two different waveguides 1 and 2 are brought together and allowed to interact linearly, two important consequences follow. The

dominant effect is that the waveguides couple via the coupling parameters  $\kappa_{12}$  and  $\kappa_{21}$ , and the secondary effect is that their respective propagation constants change as well, as shown in the Fig. 2(b) schematic. Their mode amplitudes are then governed by the coupled mode equations

$$\begin{aligned} -i \frac{d\psi_1}{dz} &= \gamma_1 \psi_1 + \kappa_{12} \psi_2, \\ -i \frac{d\psi_2}{dz} &= \kappa_{21} \psi_1 + \gamma_2 \psi_2, \end{aligned} \quad (6)$$

where  $\kappa_{ij}$  represents coupling between waveguides, and  $\gamma_j \neq \beta_j$  due to the presence of the neighboring waveguide. Both  $\kappa_{ij}$  and the  $\gamma_{ij}$  are generally functions of  $z$  (e.g., if the waveguide profiles vary).

The supermodes and propagation constants in the coupled mode picture can be obtained by determining the eigenvectors and eigenvalues of Eqs. (6). The eigenmodes take the form  $\psi_j = \tilde{\psi}_j \exp(i\tilde{\beta}_j z)$ , which have propagation constants

$$\tilde{\beta}_j = \bar{\gamma} \pm \sqrt{\kappa_{12}\kappa_{21} + \Delta_\gamma^2}, \quad (7)$$

where we have defined

$$\bar{\gamma} = (\gamma_1 + \gamma_2)/2, \quad (8)$$

$$\Delta_\gamma = (\gamma_1 - \gamma_2)/2. \quad (9)$$

The mode fields of the supermodes associated with  $\tilde{\beta}_j$ , shown in Fig. 2(c), are nominally sum and difference superpositions of the mode fields associated with the isolated (uncoupled) waveguides,<sup>54</sup> provided that the isolated modes are orthogonal to each other (i.e.,  $C_{12} \approx C_{21} \approx 0$ ). This representation of the supermodes in terms of superposition of individual waveguides modes is not valid when the waveguides are very close to each other.

## B. Eigenmode picture

An alternate picture of the two-waveguide configuration is that it supports two orthogonal eigenmodes (or “supermodes”), which form a complete basis for the current problem, as shown in the schematic of Fig. 2(c). The electric field inside the device under steady-state conditions can then be written as

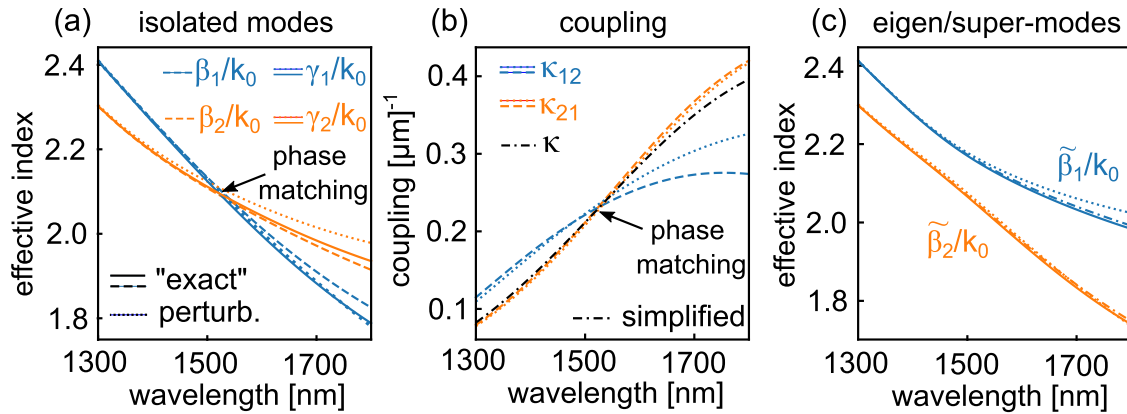


**FIG. 3.** Summary of the propagation constants and coupling parameters for the lossless case. (a) Effective index  $n_{\text{eff}} = \beta/k_0$  as a function of wavelength for the isolated modes of the geometry shown in Fig. 2(a) in the absence of losses. The blue and orange dashed lines refer to the isolated plasmonic and dielectric modes, respectively. Note the phase matching point at  $1.55 \mu\text{m}$ . The dotted lines and dashed lines, respectively, show  $\gamma_i/k_0$  using the perturbative CMT approach and the “exact” CMT approach. (b) Associated coupling coefficients. The dotted lines and dashed lines, respectively, show the results obtained from the perturbative approach using the overlap integrals in (12) and the “exact” approach by solving (15). The black dash-dotted line is obtained from the simple expression in (25). All lines cross at the phase matching point. (c) Calculated effective indices of the supermodes. The solid, dash-dotted, and dotted lines refer to the corresponding hybrid eigenmodes calculated either exactly, or via (7), or via (21), respectively.

$$\begin{aligned} \mathbf{E}(x, y, z) &= a_1 \tilde{\mathbf{E}}_1(x, y) \exp(i\tilde{\beta}_1 z) + a_2 \tilde{\mathbf{E}}_2(x, y) \exp(i\tilde{\beta}_2 z), \\ \mathbf{H}(x, y, z) &= a_1 \tilde{\mathbf{H}}_1(x, y) \exp(i\tilde{\beta}_1 z) + a_2 \tilde{\mathbf{H}}_2(x, y) \exp(i\tilde{\beta}_2 z), \end{aligned} \quad (10)$$

where  $\tilde{\mathbf{E}}_i$  and  $\tilde{\mathbf{H}}_i$  are the normalized transverse electric- and magnetic-field profiles of the eigenmodes,  $\tilde{\beta}_i$  is the eigenmode propagation constant, and  $a_i$  are amplitudes to be determined. The eigenmode picture of (10) contains the exact supermodes of the full system, while the coupled mode picture of (6) describes how two isolated modes couple when the waveguides are brought closer together.

In the EM picture, modes are also normalized such that that  $\tilde{C}_{11} = \tilde{C}_{22} = 1$ , where

$$\tilde{C}_{ij} = \hat{z} \cdot \int \int \frac{1}{2} [\tilde{\mathbf{E}}_i \times \tilde{\mathbf{H}}_j] dx dy. \quad (11)$$

For the coupled waveguide system, the index “1” and “2” simply refer to two supported supermodes in descending order of propagation constant magnitude. For the 1D modes considered in Fig. 2(a),  $\beta_j$  and the associated isolated modes’ electric and magnetic fields can be obtained by numerically solving a transcendental equation<sup>55</sup> to arbitrary numerical precision, and which can thus be considered as the “exact” solution. The same holds for the supermodes of the system of Fig. 2(c), and the solid lines in Fig. 3(c) show the exact eigenmodes of the coupled waveguides when the edge-to-edge separation is  $d = 400 \text{ nm}$  (leaving all other parameters unchanged from the previous analysis), all showing a characteristic anticrossing, or splitting, at the phase matching point.

#### IV. THE COUPLED MODE PARAMETERS

We now discuss how to explicitly obtain the parameters  $\kappa_{ij}$  and  $\gamma_i$ . Three methods can be used: (i) a perturbative approach which assumes the neighboring waveguide as a perturbation to each isolated waveguide;<sup>45</sup> (ii) an exact approach that uses only exact fields and propagation constants;<sup>42</sup> (iii) a simplified approach that uses heuristic approximations that guide physical insight.<sup>54</sup> We now consider and compare each case in detail for the plasmonic waveguide couplers.

Note that perturbative and exact approaches, as presented below, can be used for both lossless and lossy systems. Simplified approaches require instead that lossless and lossy systems be considered one at a time, as we will show.

#### A. Perturbative approach

Perturbative approaches in coupled mode theory have many incarnations—see Refs. 23 and 46 for comprehensive reviews in the context of lossless waveguides. In the limit of weak coupling, an early and frequently used perturbative treatment<sup>47</sup> yields

$$\kappa_{ij} = \frac{\omega \epsilon_0}{4} \iint [\epsilon(x, y) - \epsilon_j(x, y)] (\mathbf{E}_i^t \cdot \mathbf{E}_j^t - E_i^z E_j^z) dx dy, \quad (12)$$

where  $\epsilon(x, y)$  is the permittivity distribution of the full (coupled) system,  $\epsilon_j(x, y)$  is the permittivity distribution for the isolated waveguide  $j$ , and  $\mathbf{E}_i = \mathbf{E}_i^t + \hat{z} E_i^z$  is the electric field associated with  $\beta_i$ . We note that (12) suggests that  $\kappa_{21} \neq \kappa_{12}$  unless the guides are identical. The diagonal elements are given by

$$\gamma_1 = \beta_1 + \kappa_{11} \quad (13)$$

$$\gamma_2 = \beta_2 + \kappa_{22}. \quad (14)$$

Note that (12) immediately suggests that the diagonal elements of the matrix  $\kappa_{ij}$  matrix (being proportional to the square of the evanescent tails) are much smaller than the off diagonal elements (being linearly proportional to the evanescent tail). The dotted lines in Fig. 3(a) show the calculated  $\gamma_1$  and  $\gamma_2$  as a function of wavelength using the perturbative approach. The dotted lines in Fig. 3(b) show  $\kappa_{12}$  and  $\kappa_{21}$  using the same approach, revealing that  $\kappa_{12} = \kappa_{21}$  when the waveguides phase-match. These results can now be used to evaluate the accuracy of the perturbative CMT model in predicting the eigenvalues of the coupled system, shown in the dash-dotted lines in Fig. 3(c). The exact eigenvalues (solid lines) and the eigenvalues predicted by CMT are within  $\lesssim 1\%$  over the entire bandwidth. Note that (12) for  $k_{ij}$  is the simplest available expression. Further corrections to  $\gamma_i$  and  $\kappa_{ij}$  require more

advanced perturbative treatments, leading to increasingly complicated equations,<sup>45</sup> in extreme cases even requiring iterative algorithms.<sup>56</sup> The common tendency at this stage is to improve the perturbative CMT model further,<sup>45,56</sup> via a series of increasingly complicated overlap integrals akin Eq. (12). We have performed such calculations to find that, at least for plasmonic waveguides, improvements are negligible, and not worth the effort—such results are not shown here to avoid further clutter to Fig. 3.

## B. Exact CMT approach (CMT<sub>e</sub>)

We now present the “exact” approach in coupled mode theory (labeled as CMT<sub>e</sub>), and discuss briefly why all such perturbative treatments fail in the context of plasmonic waveguides, even in the lossless case. Indeed, knowledge of the exact transverse fields of the isolated modes and supermodes can be used to calculate the coupling parameters exactly. This approach, reported in 1985 by Hardy and Streifer in the Appendix F of Ref. 42 has had, to our knowledge, no significant uptake in the community. Nevertheless, we believe it to be extremely useful in a contemporary setting given the ubiquity of numerical solvers. Explicitly,  $\kappa_{ij}$  and  $\gamma_j$  can be obtained by solving

$$\begin{pmatrix} u_1 & v_1 & 0 & 0 \\ 0 & 0 & u_1 & v_1 \\ u_2 & v_2 & 0 & 0 \\ 0 & 0 & u_2 & v_2 \end{pmatrix} \begin{pmatrix} \gamma_1 \\ \kappa_{12} \\ \kappa_{21} \\ \gamma_2 \end{pmatrix} = \begin{pmatrix} \tilde{\beta}_1 u_1 \\ \tilde{\beta}_1 v_1 \\ \tilde{\beta}_2 u_2 \\ \tilde{\beta}_2 v_2 \end{pmatrix}, \quad (15)$$

where

$$v_m = (I_{m2} - C_{21}I_{m1})/(1 - C_{12}C_{21}), \quad (16)$$

$$u_m = (I_{m1} - C_{12}I_{m2})/(1 - C_{12}C_{21}), \quad (17)$$

and where  $I_{m1}$ ,  $I_{m2}$  are overlap integrals between individual modes and supermodes

$$I_{m1} = \hat{z} \cdot \frac{1}{2} \int \tilde{\mathbf{E}}_m \times \mathbf{H}_1 \, dx \, dy, \quad (18)$$

$$I_{m2} = \hat{z} \cdot \frac{1}{2} \int \tilde{\mathbf{E}}_m \times \mathbf{H}_2 \, dx \, dy, \quad (19)$$

having normalized each mode such that  $C_{11} = C_{22} = \tilde{C}_{11} = \tilde{C}_{22} = 1$ , and ignoring any residue field terms as per Ref. 42.

The solid blue and orange lines in Fig. 3(b), respectively, show  $\kappa_{12}$  and  $\kappa_{21}$ . We notice good agreement with the perturbative treatment for  $\kappa_{21}$  over the entire frequency range, but not so for  $\kappa_{12}$ , especially at longer wavelengths. The reason for this is immediately clear by inspecting the perturbative integral for  $\kappa_{12}$  in (12) and recalling that the permittivity of gold is nearly 50 times greater than that of the silica background: the treatment here fails because metals give rise to a strong perturbation. This effect is worse at longer wavelengths where the evanescent field of the dielectric mode has a higher overlap with the metal region and the gold permittivity increases in modulus. We conclude that perturbative treatments for obtaining the matrix elements of (6) for plasmonic waveguides in most practical settings should thus always be used with great caution. We will avoid them entirely for the remainder of this paper.

## C. Simplified CMT approach (CMT<sub>s</sub>)

The benefit of using increasingly accurate expressions in predicting how realistic PICs perform by using CMT approaches is not immediately obvious: in a realistic device, besides the inherent failure of the perturbative approach that we have just described, other issues such as edge reflections, coupling to radiation modes, or similar, might also render the CMT approach inappropriate. Furthermore, performing overlap integrals using field distributions that are confined to deep subwavelength spatial regions, as is often the case in plasmonic waveguide scenarios, is a somewhat tedious and time-consuming task. Given that advanced numerical software tools exist (e.g., COMSOL, Lumerical, CST) and that multi-core, high-performance computers with hundreds of GB of RAM are readily available to many researchers, it might be more practical to model waveguides using full numerical methods instead of going through the tedious task of implementing (12) (or more complicated versions thereof<sup>45,56</sup>), especially when dealing with 3D devices supporting 2D modes. However, such approaches are still computationally demanding, and would ideally be preceded by an intuitive framework to pinpoint the salient characteristics of a given device within the available parameter space.

While overlap integrals are widely used in CMT, they are fundamentally an uncontrolled approximation which serve a specific purpose: to find key parameters that define the full system’s behavior, determining the correct coupling constants in order to predict how waveguides interact and how power is exchanged between them. Driven by the above practical considerations, we therefore ask the question: can we instead *simplify* the two-waveguide system to its essence, via a heuristic model that requires no overlap integrals at all, and still obtain quantitatively meaningful information that can be useful as first steps in various device designs?

## D. Lossless case

We begin by considering the lossless case, which “switches off” the imaginary part of all propagation constants, so that  $\beta_i = \Re(\beta_i)$ . The first assumption of the simplified approach is that diagonal elements of  $\kappa_{ij}$  are zero, corresponding to the assumption that neighboring waveguide has a negligible effect on the other waveguide’s propagation constant, so that  $\gamma_i = \beta_i$ . Next, it uses the fact that in the lossless case power conservation leads to  $\kappa_{12} = \kappa_{21}^*$ <sup>31</sup>—recalling that for longitudinally invariant waveguides and in the absence of loss, the phase can be adjusted to make them both real, so that  $\kappa_{12} = \kappa_{21} = \kappa$ . Finally, it takes these two criteria to hold independently of the waveguide characteristics, so that the coupled mode equations simplify to

$$\frac{d}{dz} \begin{pmatrix} \psi_1 \\ \psi_2 \end{pmatrix} = i \begin{pmatrix} \beta_1 & \kappa \\ \kappa & \beta_2 \end{pmatrix} \begin{pmatrix} \psi_1 \\ \psi_2 \end{pmatrix}, \quad (20)$$

and the eigenvalues of the coupled supermodes are

$$\tilde{\beta}_j = \bar{\beta} \pm \sqrt{\kappa^2 + \Delta^2}, \quad (21)$$

where

$$\bar{\beta} = (\beta_1 + \beta_2)/2, \quad (22)$$

$$\Delta = (\beta_1 - \beta_2)/2. \quad (23)$$

Equation (21) now immediately provides a pathway for estimating  $\kappa$  after calculating the exact isolated and hybrid modes  $\beta_{1,2}$  and  $\tilde{\beta}_{1,2}$ , e.g., with any reduced-dimension mode solver, by re-writing it as

$$\kappa = \sqrt{\tilde{\Delta}^2 - \Delta^2}, \quad (24)$$

where we have defined

$$\tilde{\Delta} = (\tilde{\beta}_1 - \tilde{\beta}_2)/2. \quad (25)$$

Following this approach, the need for overlap integrals disappears completely, since it only relies on the exact propagation constants of the isolated and coupled modes. The black dash-dotted line in Fig. 3(b) shows  $\kappa$  obtained from (24) using the exact  $\tilde{\beta}_{1,2}$  and  $\beta_{1,2}$  shown in Figs. 3(c) and 3(a), respectively. We notice that  $\kappa$  lies between  $\kappa_{12}$  and  $\kappa_{21}$ , with  $\kappa_{12} = \kappa_{21} = \kappa$  at the phase-matching point. The associated  $\tilde{\beta}_i$ , obtained via the simplified equation (21), is comparable to that obtained via (7), which uses overlap integrals. This approach thus reduces a directional coupler to its essence, needing only two propagation constants and one coupling coefficient, all without overlap integrals. Previous work in the case of a lossless adiabatic couplers<sup>54</sup> has already shown that the simplifying assumption that  $\kappa_{12} = \kappa_{21} = \kappa$  provides excellent estimates of the coupling performance, even in complicated systems, when compared with full field calculations. We now continue with that approach, presenting its properties in the context of plasmonic waveguide couplers. In order to do so, we must first introduce the effects of losses due to the metal.

### E. Lossy case

Following an earlier approach,<sup>57</sup> we introduce loss in the simplified model by “switching on” the imaginary part of the gold permittivity. This modifies the propagation constant of  $\beta_2$  to be complex, while all other parameters remain the same. In other words, we take the imaginary part of  $\beta_2 = \beta_2^R + i\beta_2^I$  to be the dominant perturbation, with all other parameters unchanged from the lossless case. Equation (20) then takes the form

$$\frac{d}{dz} \begin{pmatrix} \psi_1 \\ \psi_2 \end{pmatrix} = i \begin{pmatrix} \beta_1 & \kappa \\ \kappa & \beta_2^R + i\beta_2^I \end{pmatrix} \begin{pmatrix} \psi_1 \\ \psi_2 \end{pmatrix}, \quad (26)$$

where  $\kappa$  has the same value as in the lossless case, previously obtained via (24). The eigenvalues of the lossy system are still given by (21),

replacing  $\beta_2 \rightarrow \beta_2^R + i\beta_2^I$ . In the case where the dielectric waveguide is lossy,  $\beta_1$  is also complex and  $\beta_1 \rightarrow \beta_1^R + i\beta_1^I$ . Note that because the loss of dielectric is orders of magnitude lower than metal, the inclusion of dielectric losses in the model has limited effect for most applications.

Figure 4(a) shows the real part of the effective index of each mode of this lossy system, and Fig. 4(b) shows the corresponding imaginary parts. The isolated (uncoupled) eigenmodes are again shown as dashed curves: with respect to Fig. 3(a),  $\Re(\beta_2)$  is slightly shifted due to the perturbation introduced by loss, and  $\Im(\beta_2)$  is non-zero, as expected. The dash-dotted lines in Fig. 4 shows  $\tilde{\beta}_i$  obtained from (21) using the lossy uncoupled modes  $\beta_i$  (dashed lines), and the previously obtained values of  $\kappa$  [Fig. 3(b)]. The propagation constants of the two “exact” supermodes are overlaid as dark solid curves. We find that the eigenmodes obtained with the CMT<sub>s</sub> model are in good agreement with the exact solutions.

The discrepancy between the exact eigenmodes and those predicted by the CMT<sub>s</sub> model is expected to increase as the coupling between the waveguides increases which, for example, occurs when the waveguides are brought closer together. To quantify the discrepancy, in Fig. 5(a) we plot the exact supermodes  $\tilde{\beta}_1$  (blue line) and  $\tilde{\beta}_2$  (orange line) at  $\lambda = 1.55 \mu\text{m}$  as a function of separation  $s$  and normalized to the free space wavenumber in the lossless case. The normalized propagation constant of the phase matched uncoupled modes  $\beta_{PM}$  is shown as a gray line. The corresponding eigenmodes predicted by the CMT<sub>s</sub> model are shown as dashed lines: we note that the difference start to be significant only at  $s < 200 \text{ nm}$ . To quantify the associated coupling strength relative to the propagation constant, Fig. 5(b) shows  $\kappa/\beta_{PM}$  as a function of  $s$ , showing that the CMT<sub>s</sub> model is valid in regions  $\kappa/\beta_{PM} < 0.1$ . We repeat the same analysis for the modes of lossy coupler (Fig. 4), showing the corresponding real and imaginary propagation constants in Figs. 5(c) and 5(d), respectively. We observe the same overall behavior, namely, that the eigenmodes emerging from the lossy CMT<sub>s</sub> model of Eq. (26) deviate from the exact solution for  $s < 200 \text{ nm}$ , i.e.,  $\kappa/\beta_{PM} > 0.1$ . This suggests that any CMT models should not be relied upon for accurate quantitative analyses of device performance if  $\kappa/k_0 > 0.1$ .

It is also worth considering how losses impact the predictions from Eq. (26). To illustrate this, we consider the lossy 1D waveguide

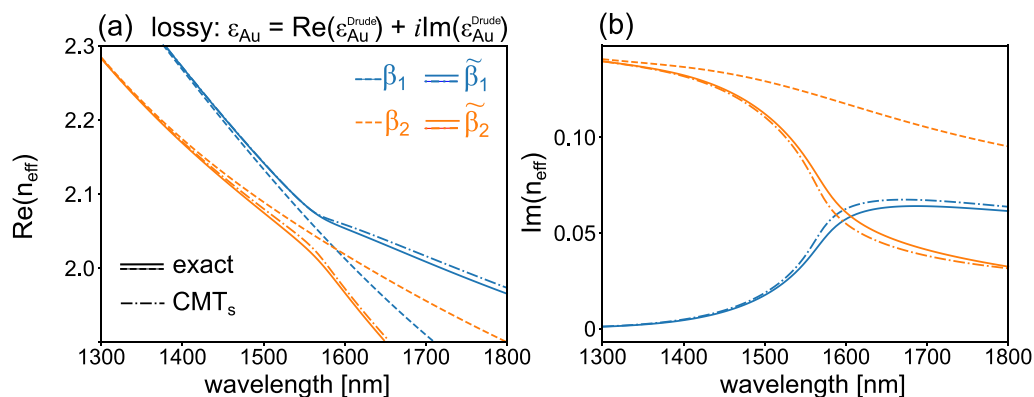


**FIG. 4.** Summary of the lossy case. (a) Real part of the effective index  $\Re(n_{\text{eff}}) = \Re(\beta/k_0)$  as a function of wavelength for modes of the geometry shown in Fig. 2 including loss. The blue and orange dashed lines show the isolated plasmonic and dielectric modes, respectively. The solid and dash-dotted lines, respectively, show the corresponding hybrid eigenmodes calculated exactly and via (7) using  $\kappa$  from Fig. 3(b) and taking  $\beta_2 = \beta_2^R + i\beta_2^I$ . (b) Corresponding imaginary part of the effective index  $\Im(n_{\text{eff}}) = \Im(\beta/k_0)$ .



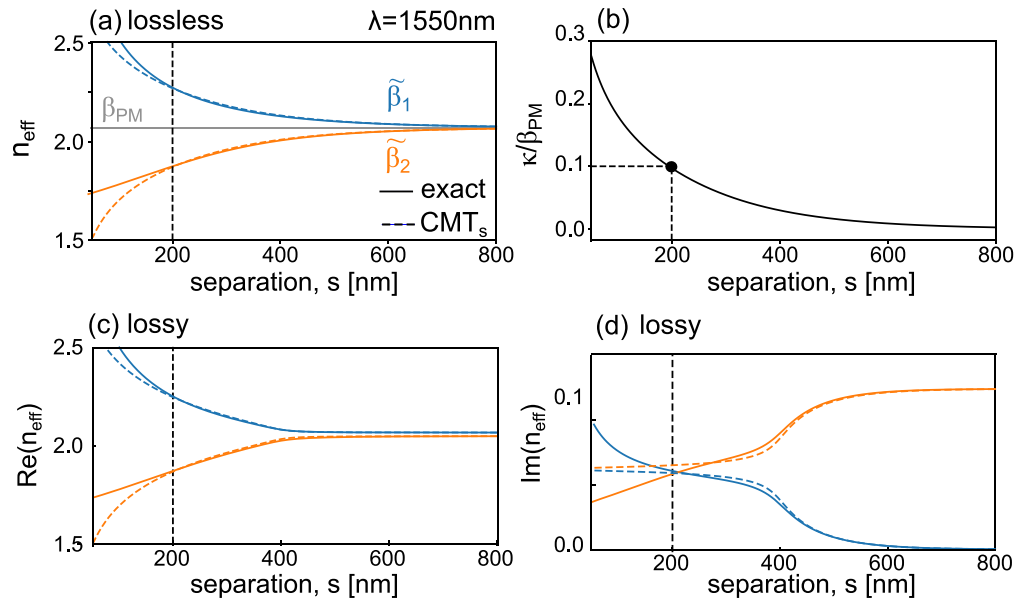


**FIG. 5.** (a) Comparison between the effective index of the exact eigenmodes (solid lines) and the  $\text{CMT}_s$  model (dashed lines), for the lossless case, as a function of the edge-to-edge separation  $s$ . (b) Corresponding  $\kappa$ , normalized to the phase-matched propagation  $\beta_{\text{PM}}$  (grey line). Note that the  $\text{CMT}_s$  model starts to break down for  $\kappa/\beta_{\text{PM}} > 0.1$  (black dashed lines). Corresponding calculations for the real and imaginary parts of the normalized eigenmodes in the lossy case are shown in (c) and (d), respectively, displaying the same overall behavior observed for the lossless case. Note in particular, the good accuracy of  $\text{CMT}_s$  for the imaginary  $\beta$ , unless the coupling is very strong.

system discussed so far at  $\lambda = 1550$  nm, taking  $s = 200$  nm where coupling is strong but the  $\text{CMT}_s$  model is applicable. The permittivity of gold is  $\epsilon_{\text{Au}} = -93 + 11i$ <sup>52</sup> corresponding to  $|\epsilon_m| = 94$  and a loss tangent  $\tan \delta = \Im m(\epsilon_m)/\Re e(\epsilon_m) = -0.12$ . We now show how the  $\text{CMT}_s$  model is affected by increasing the loss leaving all other parameters unchanged. The dash-dotted lines in Fig. 6 show the calculated  $\beta_i$  for the isolated modes as a function of  $\theta = \pi - \delta$ , so that  $\theta = 0$  corresponds to the lossless case and increasing  $\theta$  appropriately rotates the metal permittivity  $\epsilon_m$  in the complex plane. Note that  $\Re e(\beta_2)$  decreases and  $\Im m(\beta_2)$  increases, while  $\beta_1$  is unchanged. The dashed lines show  $\tilde{\beta}_i$  using the  $\text{CMT}_s$  model for a constant  $\kappa = 0.1$  [dashed line in Fig. 5(b)], which agree with the exact solutions (solid lines) up to approximately  $\theta = 0.3$ , corresponding to  $\tan \delta \approx -0.3$ . This is a loss value well above that of gold (black dotted line), consistently with our analysis so far. Furthermore, we notice that the model appears to work remarkably well even for very large values of the loss tangent. This is due to the fact that the short-range surface plasmon mode has a relatively low fraction of the field in the metal. Our approach can therefore be used for other commonly used metals, such as silver ( $\tan \delta \approx -0.08$ ), aluminum ( $\tan \delta \approx -0.18$ ), and copper ( $\tan \delta \approx -0.08$ ), by including metal dispersion<sup>52</sup> in the mode calculations as needed.

To confirm this, we repeat the above calculation assuming a lossless metal ( $\epsilon_m = -94$ ) but increasing the loss tangent of the dielectric such that  $\epsilon_d = 3.5^2 \exp(i\delta)$ , so that  $\beta_1 \rightarrow \beta_1^R + i\beta_1^I$  in Eq. (20). The results are shown in Fig. 6(b): here, the real part of the exact eigenmodes agree with those predicted by  $\text{CMT}_s$  up to  $\delta \sim 0.1$ , whereas their imaginary parts agree only for extremely modest losses. This is because more of the field is in the dielectric core, and the eigenmodes are thus more susceptible to perturbations. Our perturbative approach of taking

loss as the eigenvalue perturbation is thus ideally suited for plasmonic modes, where the field is predominantly located outside of the lossy metal region.

## V. EXPRESSION FOR THE POWER IN EACH MODE

All approaches presented so far reveal that the real parts of the supermodes anti-cross, as shown in Figs. 3(c) and 4, so that their phases advance at different rates. This is a necessary condition for achieving a large extinction in the dielectric mode due to destructive interference between the supermodes in the dielectric region, and a large fraction of power in the plasmonic mode.<sup>57,58</sup> However, in the lossy case, the device length at which each of these effects takes place is not immediately obvious, because of the complicated loss profile that emerges from each eigenmode as per Fig. 4(b). We must therefore now consider the issue of coupler performance in detail. There are several pathways for quantitatively calculating the power in each waveguide as a function of  $z$ ,<sup>24,25</sup> and one of the goals of this work is to quantitatively compare each method. In order to do so, we first review some expressions that have been used to estimate the amount of power in each waveguide. Since in most plasmonic waveguide couplers light originates in the dielectric waveguide, we take all the power to be in the dielectric waveguide at  $z=0$ , although this can be adapted as needed.

### A. Coupled mode theory approaches

In the coupled mode picture, the longitudinal power flow for each mode  $j$  in (4) can be immediately obtained from the  $z$ -component of the Poynting vector, yielding

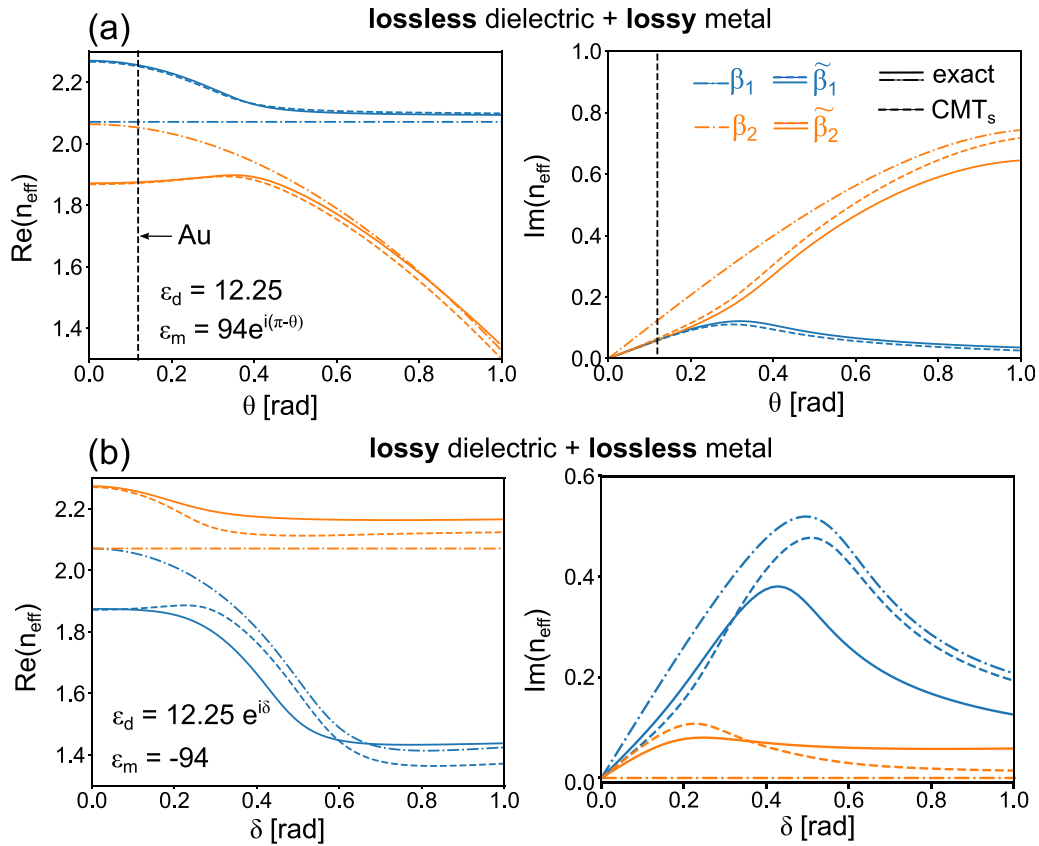


**FIG. 6.** Effect of the loss on the  $\text{CMT}_s$  model. (a) Comparison between the coupled eigenmodes as a function of  $\theta = \pi - \delta$  at the phase matching point predicted by the exact model (solid lines) and  $\text{CMT}_s$  model (dashed lines) from the isolated modes (dash-dotted lines) and  $\kappa$  obtained from the lossless case, modifying the complex metal permittivity. Here the dielectric core is lossless and the metal is lossy. (b) Analogous calculations for a lossy dielectric core and lossless metal as a function of  $\delta$ . See main text for model details.

$$P_j(z) = |\psi_j(z)|^2 \hat{z} \cdot \int \int \frac{1}{2} \text{Re} [\mathbf{E}_j(x, y) \times \mathbf{H}_j^*(x, y)] dx dy = |\psi_j(z)|^2 S_j, \quad (27)$$

where  $S_j$  is the power contained in each isolated mode following the normalization of (5). In the lossless case the normalization leads to  $S_j = 1$ , and  $P_1(z) = |\psi_1(z)|^2$ . Remarkably, we find that in the lossy case, the power contained in the plasmonic mode is  $S_2 = 1$  to within 0.6% over the entire wavelength range considered, so that  $P_2(z) = |\psi_2(z)|^2$  to good approximation. Therefore, we simply need to solve the coupled mode Eqs. (6). We take the input to be  $\psi_1(0) = 1$  and  $\psi_2(0) = 0$ , so that  $\psi_1(z)$  and  $\psi_2(z)$  are given by<sup>31</sup>

$$\psi_1(z) = \left[ \cos(\gamma_0 z) - i \frac{\Delta_\gamma}{\gamma_0} \sin(\gamma_0 z) \right] \exp(i\bar{\gamma}z), \quad (28)$$

$$\psi_2(z) = \frac{\kappa_{21}}{\gamma_0} \sin(\gamma_0 z) \exp(i\bar{\gamma}z), \quad (29)$$

where we have defined  $\gamma_0 = \sqrt{\kappa_{12}\kappa_{21} + \Delta_\gamma^2}$ . For completeness and clarity, we include the solutions to the simplified coupled mode equations of (26), which are

$$\psi_1(z) = \left[ \cos(\beta_0 z) - i \frac{\Delta}{\beta_0} \sin(\beta_0 z) \right] \exp(i\bar{\beta}z), \quad (30)$$

$$\psi_2(z) = \frac{\kappa}{\beta_0} \sin(\beta_0 z) \exp(i\bar{\beta}z), \quad (31)$$

where  $\beta_0 = \sqrt{\kappa^2 + \Delta^2}$ . In the lossless case and at the phase matching point,  $\Delta = 0$  so that  $|\psi_1(z)|^2 = \cos^2(\kappa z)$  and  $|\psi_2(z)|^2 = \sin^2(\kappa z)$ , as expected for a perfectly balanced coupler. Note that all parameters in (28) and (29) are generally complex numbers if one of the waveguides is lossy, but  $\kappa$  is always real. For more complicated cases which consider  $z$ -dependent waveguide profiles, numerical approaches are necessary.

### B. Eigenmode approaches

Another option, used in the case of longitudinally invariant waveguides,<sup>59</sup> is to use the fields and propagation constants of the exact eigenmodes.<sup>25,59</sup> To show this explicitly, it is worth re-introducing the electric and magnetic fields  $\mathbf{E}_i$ ,  $\mathbf{E}_j$  and  $\mathbf{H}_i$ ,  $\mathbf{H}_j$  associated with a given mode, schematically shown in Fig. 2. For example, in the case of 1D modes propagating along  $z$ , the total electric and magnetic fields are written as

$$\begin{aligned} \mathbf{E}(x, z) &= a_1 \tilde{\mathbf{E}}_1(x) \exp(i\tilde{\beta}_1 z) + a_2 \tilde{\mathbf{E}}_2(x) \exp(i\tilde{\beta}_2 z), \\ \mathbf{H}(x, z) &= a_1 \tilde{\mathbf{H}}_1(x) \exp(i\tilde{\beta}_1 z) + a_2 \tilde{\mathbf{H}}_2(x) \exp(i\tilde{\beta}_2 z), \end{aligned} \quad (32)$$

where  $a_i$  are the modal amplitudes which determine the contribution of the respective EMs to the total field. The complex modal amplitudes are given by<sup>59,60</sup>

$$a_i = \frac{1}{2} \int [\tilde{\mathbf{E}}_i(x) \times \mathbf{H}_0(x)] dx, \quad (33)$$

where  $H_0(x)$  is the magnetic field of the isolated dielectric mode, corresponding to the field at  $z=0$ .

Since the EM approach calculates the total field along the entire device, two methods can be used to calculate the power in each waveguide: (i) calculate the total power by integrating the  $z$ -component of the Poynting vector in the half-space comprising each individual waveguide (this method is labeled as EM<sub>i</sub>); (ii) project the total field onto the isolated eigenmode of interest, and calculate its power (this method is labeled as EM<sub>p</sub>).

**Power integration.** The EM<sub>i</sub> approach is conceptually straightforward: the total power in each waveguide can be calculated by splitting the simulation space vertically into two regions, using an artificial boundary halfway between the two waveguides at  $x_b = d + s/2$ , and defining

$$\begin{aligned} P_1(z) &= \int_{-\infty}^{d+s/2} S_z(x, y) dx, \\ P_2(z) &= \int_{d+s/2}^{\infty} S_z(x, y) dx, \end{aligned} \quad (34)$$

where  $P_1(z)$  and  $P_2(z)$  are the total powers (per unit length) in the dielectric and plasmonic regions, respectively, and where  $S_z$  is the  $z$ -component of the Poynting vector of the total field. This choice of  $x_b$  then allows to estimate the fraction of power in the dielectric and gold regions,<sup>25</sup>  $p_1$  and  $p_2$ , respectively, as a function of the propagation length

$$\begin{aligned} p_1(z) &= P_1(z)/[P_1(0) + P_2(0)], \\ p_2(z) &= P_2(z)/[P_1(0) + P_2(0)], \end{aligned} \quad (35)$$

so that  $p_1(0) + p_2(0) = 1$ .

**Mode projection.** The EM<sub>p</sub> relies on calculating the transmitted amplitude by projecting this field onto the modes of each isolated waveguide via

$$t_i(z) = \frac{1}{2} \int [\mathbf{E}_i(x) \times \mathbf{H}_{tot}(x, z)] dx, \quad (36)$$

where  $\mathbf{E}_i$  is the electric field distributions of each isolated eigenmode, and where the power in the isolated waveguide mode  $i$  is taken to be  $|t_i|^2$ , which is given by<sup>59</sup>

$$\begin{aligned} |t_i|^2 &= A_i \exp(-\Im m(\tilde{\beta}_1)z) + B_i \exp(-\Im m(\tilde{\beta}_2)z) \\ &+ \{C_i \cos[2\Re e(\tilde{\Delta})z] + D_i \sin[2\Re e(\tilde{\Delta})z]\} \\ &\times \exp(-\Im m(\tilde{\beta})z), \end{aligned} \quad (37)$$

where the  $A_i, B_i, C_i, D_i$  coefficients contain only overlap integrals between the isolated- and coupled- eigenmodes [see Eq. (6) in Ref. 59

for their explicit expressions]. Equation (37) explicitly indicates that the energy exchange between waveguides is only related to the real parts of  $\tilde{\Delta}$ , i.e., to the dephasing of the eigenmodes  $\tilde{\beta}_i$ , whereas the imaginary parts of  $\tilde{\beta}_i$  influence the overall loss. Equation (37) quantitatively predicts the coupling efficiency as a function of  $z$ , provided that the overlap coefficients in (33) are known. For example, in the lossless case and at the phase matching point  $\Im m(\beta_i) = 0$  and  $\Re e(\tilde{\Delta}) = \kappa$ . If all power at  $z=0$  is in the dielectric mode, then (37) implies that the power in the plasmonic mode takes the familiar form  $|t_2|^2 \approx (1 - \cos(2\kappa z))/2 = \sin^2(\kappa z)$ <sup>45</sup> and complete power transfer occurs at  $L_c = \pi/2\kappa$ , since numerical integrals yield  $A_2 + B_2 \approx 1/2$ ,  $C_2 \approx -1/2$ , and  $D_2 = 0$ .

The advantage of the EM approaches is that they rely on the exact eigenmodes and propagation constant, and are thus more accurate than CMT approaches.<sup>24,57</sup> It should be noted that this method is most suitable to longitudinally invariant waveguides, but any transverse modifications to the waveguide upon propagation—e.g., in adiabatic couplers<sup>54</sup>—requires transfer matrix approaches (i.e., splitting the domain in smaller slices along  $z$ <sup>20,61</sup>), which can increase the computational cost via additional overlap integrals.<sup>62</sup> While the eigenvalues obtained from the CMT model have the disadvantage of deviating slightly from the exact solutions, as shown in Figs. 3 and 4, they have the remarkable advantage of providing an immediate pathway for calculating the power in devices whose spatial profile varies along  $z$ , simply by calculating  $z$ -dependent parameters  $\kappa(z)$  and  $\beta_i(z)$  which, as we have shown, can be obtained easily from reduced-mode calculations and no overlap integrals.

### C. Finite element approaches

In order to evaluate the accuracy of the above approaches, we compare the power in each waveguide with that predicted by finite element method (FEM) calculations using the commercially available software COMSOL,<sup>63</sup> which allows the user to excite a desired mode at input, and which in turn allows for two different approaches. On the one hand, it is simply possible to integrate the calculated power in each half-space, as per Eq. (34). We label this approach as FEM<sub>i</sub>. On the other hand, COMSOL has a built-in port function<sup>63</sup> that allows the user to project the output of the calculation on a desired isolated mode and obtain its power, which is conceptually equivalent to the mode projection method in Eq. (33). We label this approach FEM<sub>p</sub>. A summary of each method presented so far, and the notation used in subsequent figures, is presented in Table I.

We are now interested in comparing the *simplified* coupled mode theory approach with the eigenmode and finite element method for longitudinally invariant directional couplers and plasmonic sensors in the case of 1D modes propagating in 2D, before using CMT in more complicated and computationally demanding 2D modes propagating in 3D and with arbitrary  $z$ -dependent profiles. Since our focus is on understanding how well CMT<sub>s</sub> performs, we will be avoiding the “exact” coupled mode theory approach, since it uses the same overlap integrals as the eigenmode method (which also uses exact modes), and is therefore redundant.

## VI. DIRECTIONAL COUPLING

We begin by considering the power exchanged between the two waveguides of the *lossless* directional coupler shown in the Fig. 2 schematic. We use the same materials and refractive index distribution,

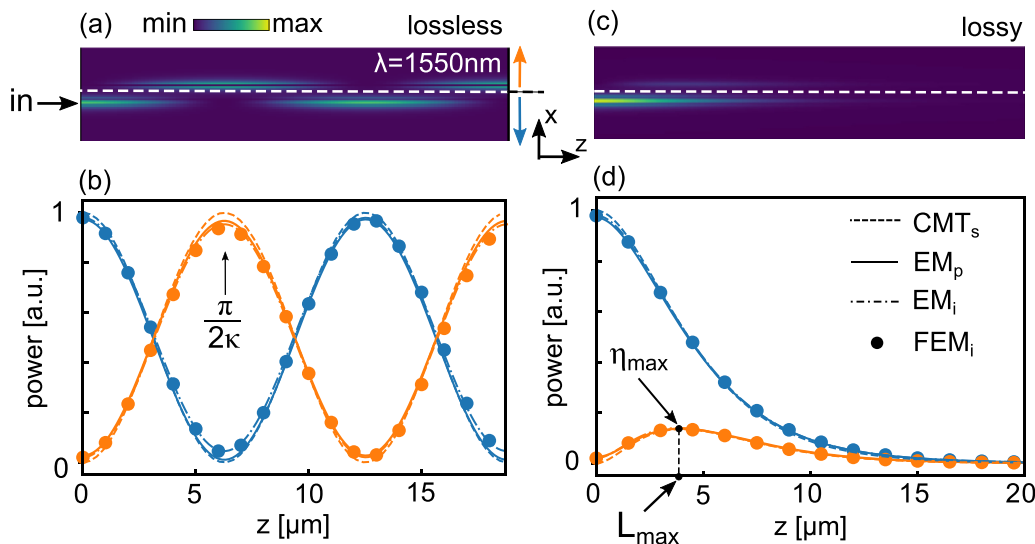
**TABLE I.** Summary of the methods used, their associated labels, equations, and salient features.

Method name	Method label	Relevant equations	Comment
“Exact” coupled mode theory	CMT <sub>e</sub>	(28) and (29)	Uses exact modes and overlap integrals.
Simplified coupled mode theory	CMT <sub>s</sub>	(30) and (31)	$\kappa$ obtained from lossless modes, no integrals.
Eigenmode method + projection	EM <sub>p</sub>	(36) and (37)	Uses exact modes and overlap integrals.
Eigenmode method + integration	EM <sub>i</sub>	(34) and (35)	Integrates power at halfway boundary.
Finite element method + projection	FEM <sub>p</sub>	N.A.	See Ref. 63 for details.
Finite element method + integration	FEM <sub>i</sub>	N.A.	Integrates power at halfway boundary.

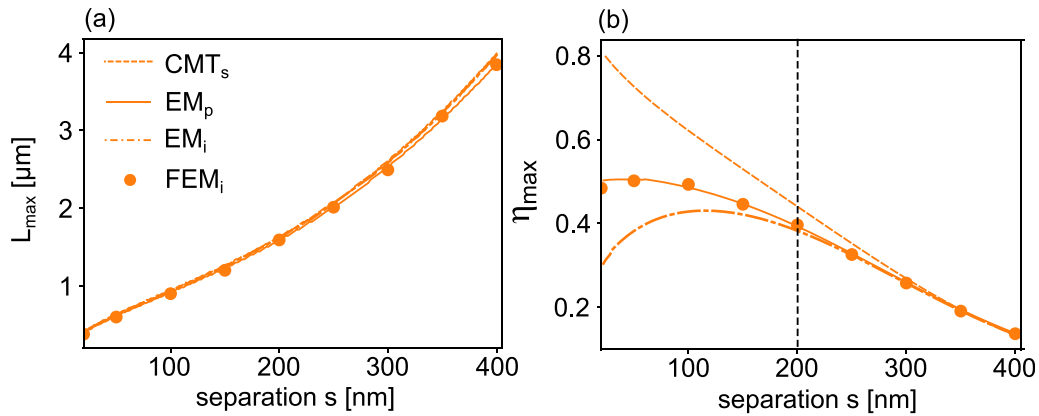
including the material dispersion for silica<sup>53</sup> and gold (Drude model in Ref. 52), setting the imaginary part of the permittivity to be zero everywhere. The dispersion of its relevant modes is shown in Fig. 2. A colormap of the power in the coupler at  $\lambda = 1550$  nm, obtained from 2D FEM<sub>i</sub> calculations, is shown in Fig. 7(a). As expected, a complete transfer of power between each waveguide occurs with a period of  $\pi/2\kappa$  obtained from Fig. 2(b), corresponding to approximately  $6 \mu\text{m}$ . The circles in Fig. 7(b) show the associated power in the plasmonic mode (orange) and dielectric mode (blue), using FEM<sub>i</sub>. A comparison with the CMT<sub>s</sub>, EM<sub>i</sub>, and EM<sub>p</sub> approaches are shown as dashed, solid, and dash-dotted lines, respectively, keeping the same color coding. The best overall agreement occurs for the EM<sub>p</sub> approach, which projects the total field on the exact eigenmodes. The other methods show excellent agreement in terms of power transfer length, but small discrepancies (<5%) in terms of coupling efficiency, as seen in Fig. 7. We now move away from the lossless directional coupler, since it has been considered extensively,<sup>43,46</sup> and discuss only the lossy case.

Figure 7(c) shows a colormap of the power obtained from FEM<sub>i</sub> calculations of the corresponding lossy coupler, whose complex modes' dispersions are plotted in Fig. 4. Figure 7(d) compares the power in each waveguide, following the same naming convention as in Fig. 7(b). Introducing loss has two effects: (i) it changes the eigenmode splitting at the phase matching point [c.f. Fig. 2(c) and Fig. 4(a)]; (ii) it leads to a plateau in the amount of power that is transferred from the dielectric mode to the plasmonic mode, as a result of a net overall absorption. Each of these effects depend on the specific device parameters, making it challenging to quantify the maximum coupling efficiency into the plasmonic mode  $\eta_{\text{max}}$  and the associated length  $L_{\text{max}}$  at which it occurs. This is in contrast to the lossless case, where  $\kappa$  is the only parameter needed to estimate the minimum power transfer length, and where the maximum transfer efficiency is always unity.

To quantitatively investigate the effect that bringing the waveguides together has on  $L_{\text{max}}$  and  $\eta_{\text{max}}$ , we repeat the above calculations for the lossy directional coupler as a function of separation  $s$ ,



**FIG. 7.** (a) Colormap of the spatial distribution of Poynting vector component in the  $z$  direction in the lossless directional coupler from Fig. 2 at  $\lambda = 1.55 \mu\text{m}$ . (b) Associated power in the dielectric waveguide 1 (blue) and plasmonic waveguide 2 (orange) using different methods described in the text. Circles: FEM<sub>i</sub> calculations; solid lines: EM<sub>p</sub> method; dash-dotted lines: EM<sub>i</sub> method; dashed lines: CMT<sub>s</sub> method. Note that the transfer length from the dielectric mode to the plasmonic mode is trivially  $\pi/2\kappa$ . For comparison, (c) and (d), respectively, show the same results as (a) and (b), but for the lossy directional coupler presented in Fig. 4. Here, the maximum transfer efficiency  $\eta_{\text{max}}$  and the associated transfer length  $L_{\text{max}}$  are non-trivial because the eigenvalues are complex. The total power at  $z=0$  is normalized to unity. Window size in (a) and (c):  $20 \mu\text{m} \times 4 \mu\text{m}$ .



**FIG. 8.** Calculated (a) transfer length  $L_{\max}$  and (b) plasmonic coupling efficiency  $\eta_{\max}$  as a function of edge-to-edge separation  $s$  between the lossy waveguides shown in Fig. 7(c). Circles: FEM<sub>i</sub> method; solid lines: EM<sub>p</sub> method; EM<sub>i</sub>; dashed lines: CMT<sub>s</sub> method.

identifying the value of  $L_{\max}$ , and  $\eta_{\max}$  in each case and for each method. Figure 8(a) plots the coupling length as a function of separation, showing remarkably excellent agreement between all methods. Figure 8(b) plots the associated efficiency  $\eta_{\max}$ : all methods agree well if the separation between waveguides is greater than 200 nm, which is the region where the eigenvalues predicted by CMT<sub>s</sub> deviate from the exact solution. The EM<sub>p</sub> method gives the best overall agreement, whereas the EM<sub>i</sub> method does not work for small separations because, in this scenario, the power in each dielectric and plasmonic half-space becomes less representative of the mode power of the corresponding uncoupled waveguide. This can easily be overcome, for example, by slowly increasing the mutual separation between waveguides (but at the cost of increasing the overall loss), as per an adiabatic device.<sup>64</sup> Finally, for strong coupling the CMT<sub>s</sub> method overestimates the coupling efficiency by a significant margin, due to the breakdown of the perturbative assumptions, and should be used with caution. From an experimental viewpoint, this is still a valuable result: the lossy CMT<sub>s</sub> approach predicts the desired device length with remarkable accuracy, which is already very important for device design prototyping. However, in the strong coupling regime where  $\kappa/\beta > 0.1$ , a comparison with full wave calculation indicates the associated coupling efficiency is inaccurate. The lack of accuracy cannot be mitigated without making the simple model more complicated. Improving the model would require, for example, the incorporation of additional modes (e.g., higher order and radiative modes), which would make the system larger, but also require a case-by-case dependent study—at which point, a full numerical solver would be the more convenient approach.

### A. An explorer's map

With this knowledge in hand, we are now in the unique position to provide a universal “explorer's map” of  $L_{\max}$  and  $\eta_{\max}$  as a function of parameters that can be easily obtained from exact mode calculations via the CMT<sub>s</sub> model, and which is agnostic to details of the waveguide cross section used. This map can be considered as universal and accurate, provided that: (a) we are at the phase matching point, i.e.,  $\Re(\beta_1) \approx \Re(\beta_2) = \beta_{\text{PM}}$ , so that  $\kappa = \tilde{\Delta}$  and (b) coupling between waveguides is not too strong, i.e.,  $\kappa/\beta < 0.1$ . Under these conditions, following (31), the expression for the power in the plasmonic waveguide is

$$|\psi_2(z)|^2 = \frac{\tilde{\Delta}^2}{\tilde{\Delta}^2 - |\beta_2^I|^2/4} \sin^2\left(z\sqrt{\tilde{\Delta}^2 - |\beta_2^I|^2/4}\right) \exp(-|\beta_2^I|z). \quad (38)$$

This expression only depends on two “exact” mode parameters: (a) the supermode splitting, here given by  $\tilde{\Delta} = (\beta_1 - \beta_2)/2$  (obtained from lossless waveguides) and (b) the imaginary part of the isolated plasmonic waveguide  $\beta_2^I$ . We consider  $|\psi_2(z)|^2$  in Eq. (38) for various combinations of  $\tilde{\Delta}$  and  $\beta_2^I$  to obtain the power in the plasmonic waveguide as a function of  $z$  [as per the orange line in Fig. 7(d)] and computing the associated  $L_{\max}$  and  $\eta_{\max}$ . The associated contour maps showing  $L_{\max}/\lambda$  and  $\eta_{\max}$  are shown in Figs. 9(a) and 9(b), respectively. As expected, the most compact and efficient devices (low  $L_{\max}$ , high  $\eta_{\max}$ ) occur when the eigenmode splitting is large and the losses are low (top left in the colormap). Vice versa, increased losses and small splittings lead to undesirably long devices ( $L_{\max} \gg \lambda$ ) that are inefficient ( $\eta_{\max} < 0.1$ ). Note that for small  $\tilde{\Delta}$ , even modest losses lead to inefficient devices, as can be seen in the bottom region of Fig. 9; in contrast, regions of strong coupling are the most efficient, even when the losses are large, as can be seen in the top region of Fig. 9.

### B. Wavelength dependence

We now consider the wavelength dependence of the CMT<sub>s</sub> model. Once again, our approach is to consider  $\kappa$  to be constant at each wavelength, and calculate it from “exact” modes via Eq. (24). To show how the model performs at the limit of its applicability, we consider  $s = 200$  nm, which is where the eigenmodes predicted by CMT<sub>s</sub> start to deviate significantly from the exact case (dashed line in Fig. 5). Figure 10(a) shows  $L_{\max}$  and  $\eta_{\max}$  in blue (left axis) and orange (right axis), respectively. The circles and solid lines show the total power contained in the plasmonic waveguide region according to FEM<sub>i</sub> and EM<sub>i</sub> methods. The CMT<sub>s</sub> method is overlaid as a dashed line: we observe that, despite its simplicity, this method faithfully reproduces all salient quantitative trends. Note that  $\eta_{\max}$  increases and  $L_{\max}$  decreases at longer wavelengths because the loss of the plasmonic mode goes down [as evident from Fig. 4(b)], and because mode coupling is stronger. Furthermore, we find that the discrepancies increase at longer wavelengths, and decrease for shorter wavelengths, despite the fact that

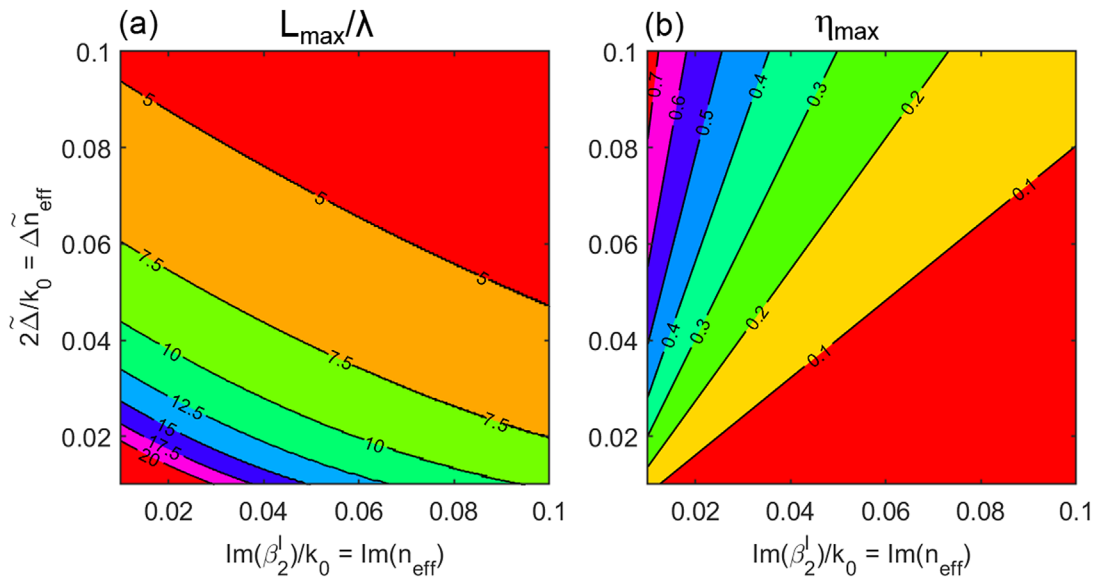


**FIG. 9.** Colormap of (a) transfer length (in units of wavelength)  $L_{\max}/\lambda$  and (b) plasmonic coupling efficiency  $\eta_{\max}$  as a function of the imaginary part of the effective index  $\Im m(n_{\text{eff}}^{(2)}) = \beta_2^l/k_0$  and  $\Delta\tilde{n}_{\text{eff}} = 2\Delta/k_0$  using CMT<sub>s</sub> via (38).

neither regions are at the phase matching wavelength of  $\lambda = 1550$  nm, where  $\kappa_{12} = \kappa_{21} = \kappa$ . A plot of  $\kappa/\beta_i$  as a function of wavelength is shown in Fig. 10(b), confirming that the modes at longer wavelengths are more strongly coupled than those at shorter wavelengths (i.e.,  $\kappa/\beta_i > 0.1$  when  $\lambda > 1550$  nm, and vice versa). All things being equal, this result indicates that weaker coupling improves the quantitative accuracy of CMT<sub>s</sub> models.

### C. Plasmonic sensing

Waveguide sensors which use surface plasmon polariton (SPP) resonances are particularly attractive for bio-sensing at the nanoscale,<sup>65</sup> because they exploit the subwavelength lateral confinement of SPPs to characterize small modifications to the environment via changes in the propagating field's phase or loss. Originally implemented using free-space bulk optics,<sup>66,67</sup> SPP sensors are ideal for integration with chip-

scale<sup>68</sup> and fiber-based<sup>30</sup> platforms, providing a monolithic and convenient way of detecting small changes near the metal surface.<sup>69–71</sup>

Figure 11(a) shows a schematic of a typical chip-scale hybrid plasmonic waveguide coupler, which is a modified version of the device shown in Fig. 2: the only difference is that the external region adjacent to the metal is now covered by an analyte (refractive index:  $n_a$ ). Light is injected into the dielectric core and couples to the plasmonic mode, yielding an overall transmission spectrum given by the power emerging from the dielectric waveguide, which of course depends on many parameters, including the wavelength  $\lambda$ , length  $L$ , and refractive index  $n_a$ .

Changes in the dielectric transmission spectra  $T(\lambda)$  are often sensitive to any changes in the refractive index above the metal film. It is therefore important to be able to calculate them accurately and for realistic experimental conditions. Recent works have shown that the overall transmission spectra for different values of  $n_a$ , calculated in

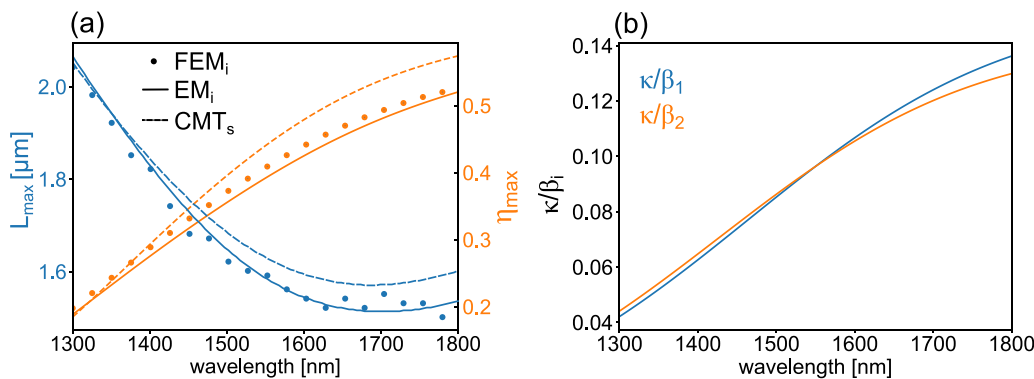


**FIG. 10.** Directional coupler bandwidth calculations. (a) FEM (circles), EM<sub>i</sub> method (solid lines) and CMT<sub>s</sub> (dashed lines) for the maximum transfer efficiency  $\eta_{\max}$  (orange, right axis) and the coupling length  $L_{\max}$  at which it occurs (blue, left axis), as defined in Fig. 4(d). (b) Associated  $\kappa/\beta_i$  for considering the isolated dielectric (blue) and plasmonic (modes).

18 April 2024 13:02:07

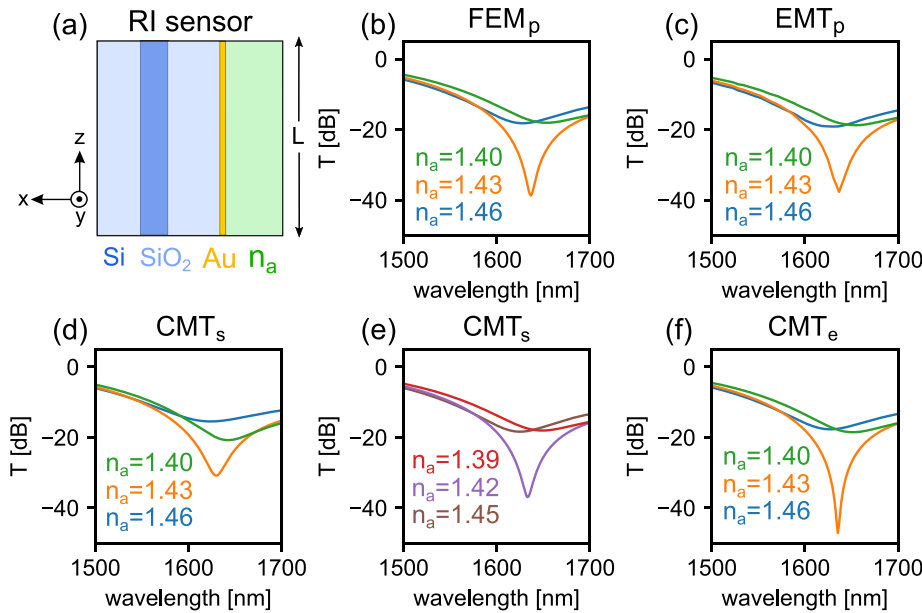


**FIG. 11.** Schematic of the plasmonic sensor. The only difference with respect to Fig. 2 is that the external region in contact with the gold film is now an analyte with refractive index  $n_a$  (green). The length  $L$  refers to the length of device in the propagation direction  $z$ . Here, we consider  $L = 10 \mu\text{m}$ . Calculated transmission spectra for  $n_a = 1.40$  (green),  $n_a = 1.43$  (orange) and  $n_a = 1.46$  (blue) are also shown, as obtained using (b) FEM<sub>p</sub>, (c) EM<sub>p</sub>, (d) CMT<sub>s</sub> approaches. (e) CMT<sub>s</sub> approach with  $n_a = 1.39$  (red),  $n_a = 1.42$  (purple) and  $n_a = 1.45$  (brown) using CMT<sub>s</sub>. FEM<sub>p</sub> and EM<sub>p</sub>, and exact CMT<sub>e</sub> approaches show good agreement, however using CMT<sub>s</sub> there is a small shift in the analyte index where the sharpest resonance dip occurs.<sup>24</sup>

Fig. 11(b) using FEM<sub>p</sub> can be well reproduced by the EM<sub>p</sub> method,<sup>57</sup> as shown in Fig. 11(c). The CMT<sub>s</sub> method [Eq. (30)] reproduces the salient properties of the coupled supermodes, but the resulting transmission spectra are systematically shifted in terms  $n_a$ , as discussed in detail in Ref. 24, and shown in the corresponding calculations of Figs. 11(d) and 11(e). This is most likely because the sharp resonances rely on destructive interference, which are sensitive to small perturbations in each eigenmode’s effective index. Although the CMT<sub>s</sub> approach can still provide ballpark figures of a sensor’s performance—and is certainly more appropriate than any other method that uses mode dispersion curves alone—accurate calculations of plasmonic sensor transmission spectra necessarily require “exact” approaches, either via the EM<sub>p</sub> method, or via the CMT<sub>e</sub> method [Eq. (28)].

Figure 11(f) shows the transmission spectrum calculated using the CMT<sub>e</sub> approach for  $z = L = 10 \mu\text{m}$ , showing good agreement with the FEM<sub>p</sub> and EM<sub>p</sub> methods—aside from predicting slightly sharper resonances at  $n_a = 1.43$ . The CMT<sub>s</sub> model might still find uses for first estimate of parameter regions where sharp resonances are expected for different choices of  $n_a$ , but methods that consider exact modes are necessary for accurate comparisons with experiments.

#### D. The exceptional point

The plasmonic couplers discussed so far all rely on a transfer of power between the dielectric and plasmonic waveguides near the phase matching point, which is due to an anti-crossing of the coupled eigenmodes. However, in lossy systems, when  $\kappa$  is too small then the real parts of the supermodes cross<sup>24</sup>—resulting in an infinite beat length, which precludes both destructive interference and sharp resonances. The boundary between regions where  $\Re(\tilde{\beta}_i)$  cross and anti-cross—and which thus separates regions where plasmonic couplers can be most efficient—corresponds to the exceptional point (EP), where the complex supermode propagation constants are degenerate, which by definition corresponds to the condition

$$\tilde{\beta}_1 - \tilde{\beta}_2 = 0. \tag{39}$$

According to CMT<sub>s</sub> (24), this condition corresponds to  $\kappa^2 + \Delta^2 = 0$ ,<sup>58,72</sup> wherein the following conditions simultaneously need to be met:

$$\begin{cases} \beta_1 - \beta_2^R = 0, \\ \kappa - \beta_2^I/2 = 0. \end{cases} \tag{40}$$

The exceptional point is thus an important parameter for plasmonic directional couplers and plasmonic sensors, because it defines the point beyond which resonant coupling is not supported. The CMT<sub>s</sub> model immediately provides a rapid way of identifying it, in terms of intuitive coupling- and loss-parameters: using this method, it is possible to verify *a priori* that the condition  $\kappa > \beta_2^I/2$  at the phase matching point is met, and then estimate the associated coupling efficiency and coupling length.

#### VII. ADIABATIC COUPLER

Directional couplers can provide high coupling efficiencies over wavelength-scale distances, but because they rely on interference effects, they tend to have a narrow bandwidth and their performance is sensitive to any fabrication imperfections. In contrast, *adiabatic* couplers<sup>64</sup> are relatively robust devices that can have a large bandwidth.<sup>54,73</sup> In the present context, the type of adiabatic coupling under consideration is illustrated in Fig. 12(a). To understand its operation, we consider the fundamental supermode of the device. Although each supermode can be thought of as a superposition of the fundamental modes of the isolated waveguides 1 and 2, the device is designed such that at  $z=0$  and  $z=L$  the fundamental supermodes  $\tilde{\psi}_{1,2}$  closely match the modes of the individual waveguides, because they are not phase matched and therefore detuned: for the device in Fig. 12(a), the fundamental supermode at  $z=0$  corresponds nominally to the isolated mode of waveguide 1, whereas at  $z=L$  it corresponds to that of the plasmonic waveguide 2. For the device in the schematic this is achieved

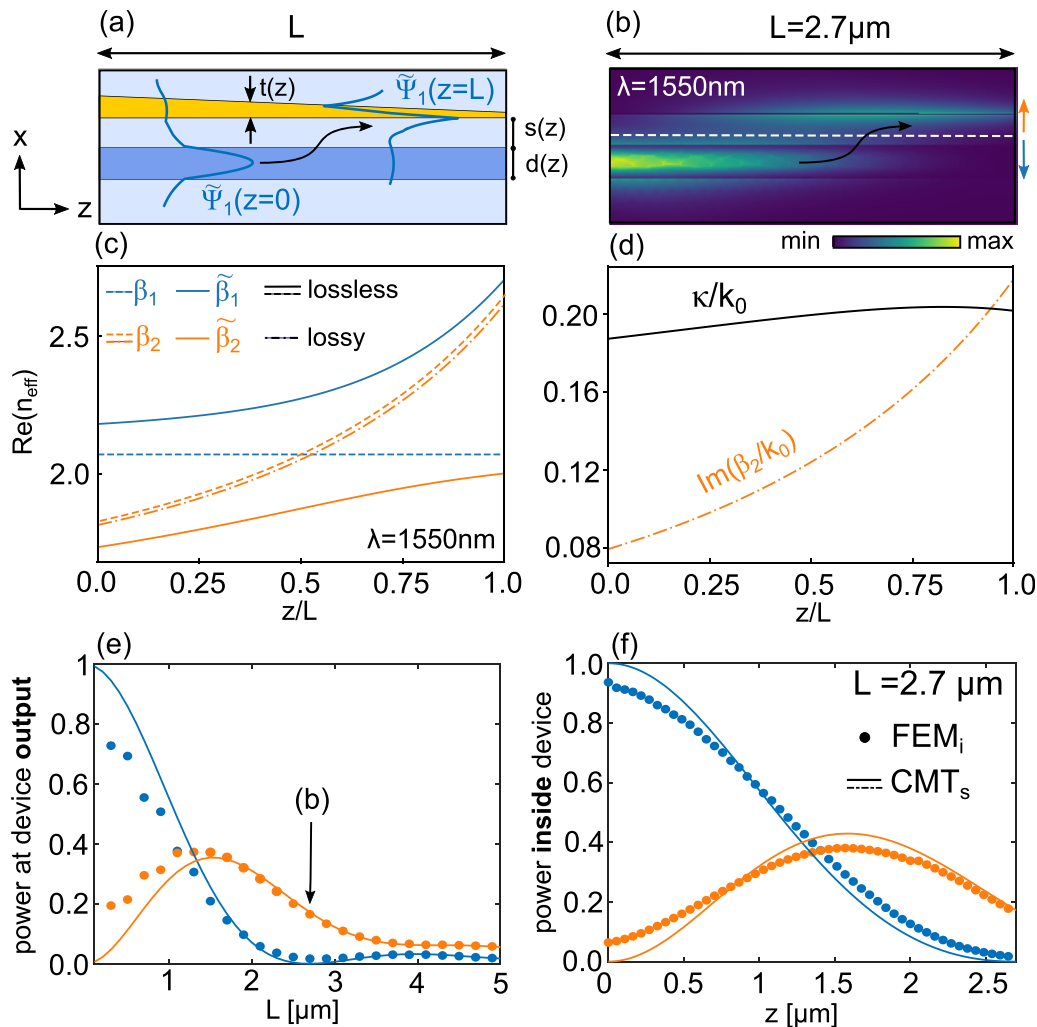


**FIG. 12.** (a) Schematic of a plasmonic adiabatic coupler. Light starts in waveguide 1, corresponding to a supermode at  $z=0$ , and remains in this mode, which at the end of the device corresponds to all the power being in waveguide 2. (b) Calculated  $z$ -component of the Poynting vector for the adiabatic waveguide described in the text when  $L = 2.7 \mu\text{m}$ . (c) Real part of the effective index as a function of  $z/L$  for the lossless supermodes (solid lines) and isolated modes (dashed lines). The dash-dotted line shows the lossy isolated plasmonic mode. Mode nomenclature and color coding is analogous to Fig. 2. (d) Associated  $\kappa$  (black line) imaginary part of the isolated plasmonic mode (orange). (e) Power at the device *output* (i.e., at  $z=L$ ), in the dielectric (blue) and plasmonic waveguide (orange), as a function of device length  $L$ , calculated using FEM<sub>i</sub> (circles) and CMT<sub>s</sub> (solid lines). (f) Corresponding  $z$ -dependent power *inside* each waveguide for a fixed  $L = 2.7 \mu\text{m}$ .

by varying the width of the plasmonic waveguides, a common approach.<sup>27</sup> Alternatively, the width of the dielectric waveguide can also vary while keeping the plasmonic waveguide constant.<sup>29</sup> In a perfectly adiabatic process, light that is coupled into the fundamental supermode enters through waveguide 1, remains in the fundamental supermode, and exits via waveguide 2 with 100% efficiency. A consequence of adiabaticity is that, provided that the supermodes coincide with each of the individual waveguides at  $z=0$  and  $z=L$ , the device performance is relatively insensitive to perturbations, wavelength, or even to the details of the device design.<sup>54,73</sup>

Adiabatic devices are therefore typically advantageous over directional couplers due to their robustness to fabrication imperfections and broad bandwidth; however, because of the requirement of

adiabaticity, they tend to achieve unity coupling efficiency over quite long lengths. This requirement can be relaxed to some degree, and many techniques have been developed that promise to minimize this length while maintaining performance.<sup>74</sup> However, such techniques are only applicable to the lossless case, where increasing the device length does not impact the overall absorption.<sup>54</sup> As a variation to our leitmotif, we now consider the case where the plasmonic waveguide profile varies as a function of the propagation distance, as illustrated in the schematic of Fig. 12(a). Even though  $s$  can be a function of  $z$ , we choose it to be constant such that  $s(z) = 200 \text{ nm}$  and only vary  $t$ , while also keeping  $d(z) = 220 \text{ nm}$  constant. Recall that the dielectric waveguide mode phase matches with the short range plasmonic mode at  $t = 7.5 \text{ nm}$ . We now harness the fact that, for SRSPPs, thinner films



yield larger propagation constants, accompanied by large group velocity and high localized field intensity on the gold surface.<sup>55,75</sup> We take  $t(z)$  to decrease linearly between 10 and 5 nm over the device length, so that the plasmonic mode crosses with the dielectric mode in the middle of the device.

We now briefly discuss how to set up and solve adiabatic plasmonic couplers using the CMT<sub>s</sub> approach. The reason for this is that the power exchange properties in plasmonic couplers are non-trivial, so that design needs may vary from case to case. For example, one might want to know how long the device should be to ensure that most power goes into the plasmonic waveguide, but for this length some power may remain in the dielectric waveguide (crosstalk).<sup>64,73</sup> Alternatively, one might want a device length such that no power is in the dielectric waveguide, harnessing all the power which happens to be in the plasmonic mode.<sup>27</sup> How long would that device have to be? How much power would be in the plasmonic mode? In the present case, time-consuming finite element calculations shown in Fig. 12(b), suggest that this occurs at a length of  $L = 2.7 \mu\text{m}$ , and that the associated  $\eta = 20\%$ . We now consider whether this result can be quantitatively obtained with the CMT<sub>s</sub> approach.

In essence, we must now solve (26) with all parameters being  $z$ -dependent. Recall that the diagonal elements of (26) are the isolated modes of the lossy device, and that  $\kappa(z)$  is obtained from (24) at constant  $\lambda$  using equivalent lossless modes. We also neglect all reflections, and consider only forward-propagating modes. Figures 12(c) and 12(d) show all parameters needed for this calculation. Dashed and solid lines show the propagation constant of the lossless isolated modes and supermodes, respectively, as a function of  $z/L$ , which result in  $\kappa(z)$  as per (24), which is plotted as a black line in Fig. 12(c). Finally, the real and imaginary parts of the complex isolated lossy mode  $\beta_2$  are shown as a dash-dotted lines in Figs. 12(c) and 12(d).

These parameters are then used to solve (26) numerically for different physical device lengths  $L$ , taking  $\psi_1(0) = 1$  and  $\psi_2(0) = 0$ , and calculating the power  $|\psi_i(L)|^2$  in each waveguide  $i$  at  $z = L$ . The solid lines in Fig. 12 shows the resulting  $|\psi_1(L)|^2$  (blue line) and  $|\psi_2(L)|^2$  (orange line) using the CMT<sub>s</sub> model. The exchange of power between waveguides is quite complicated, but in good agreement with the full finite element calculations (circles). Note in particular, that this model predicts that the maximum coupling efficiency is approximately 0.4 at  $L = 1.5 \mu\text{m}$ , with a residual power fraction of 0.2 in the dielectric waveguide. Increasing the device length further produces a reduction in the power in the plasmonic waveguide due to losses. At  $z = 2.7 \mu\text{m}$ , the power in the dielectric waveguide is at a local minimum, and the fraction of transmitted power in the plasmonic waveguide is 0.2. Our simple model also provides useful insight into how the power is distributed *within* the device for a given  $L$ . Figure 12(f) shows the power in each waveguide mode as a function of  $z$  for  $L = 2.7 \mu\text{m}$  predicted by the CMT<sub>s</sub> model (solid lines) and by FEM<sub>1</sub> (circles), both showing that in this configuration the highest power inside a device of this length occurs at  $z = 1.6 \mu\text{m}$ .

One important advantage of the CMT<sub>s</sub> approach is that it provides physical insight as to why a given coupler is performing in a certain way. Here, the near-constant  $\kappa$  [black line in Fig. 12(d)] shows that this particular choice of waveguide parameters leads to an adiabatic device that is similar to a directional coupler. Indeed, there are infinitely many choices for  $s(z)$ ,  $t(z)$ , and  $d(z)$ , each of which will yield different results, and a systematic study of the study of how different

coupler profiles and (and associated losses) might affect the performance – as has been done in the lossless case<sup>54</sup>—might be warranted. Recent work has also shown that physics-informed neural networks provide a pathway for even more rapid device optimization.<sup>76</sup> We anticipate that the present formalism, and generalizations thereof, will be very useful in that context.

## VIII. APPLICATION TO 3D WAVEGUIDES

So far, we have considered 2D waveguides supporting 1D modes, as a means of verifying the validity and limitations of CMT<sub>s</sub> for calculating the power transfer properties of plasmonic couplers. We expect our formalism and intuitive framework to be more practical for realistic 3D waveguides supporting 2D modes, which are generally quite computationally demanding to model using vector field approaches. Furthermore, field overlap integrals used in the EM and CMT<sub>e</sub> approaches are also somewhat tedious and time consuming to implement in this scenario, due to the fine mesh sizes and high spatial resolution required for accuracy. The CMT<sub>s</sub> approach, which uses eigenvalue calculations alone, is thus particularly valuable in navigating the first design steps to obtain the desired performance, especially in terms of footprint and coupling efficiency. We now discuss two canonical plasmonic geometries often used for plasmonic directional and adiabatic coupling, comparing the simplified coupled mode theory with full finite element calculations.

### A. Chip-based plasmonic coupler

We start our discussion with a metal–dielectric–metal (MDM) plasmonic waveguide coupled to a silicon-on-insulator (SOI) waveguide,<sup>77</sup> frequently used in the context of wavelength-scale couplers,<sup>78,79</sup> nonlinear light generation,<sup>27</sup> and Raman spectroscopy.<sup>80,81</sup> Figures 13(a)(i)–(ii) show a cross-sectional schematic of the device and supported mode at  $\lambda = 1.55 \mu\text{m}$ : a rectangular dielectric silicon waveguide ( $n = 3.5$ ) of width  $w = 300 \text{ nm}$  and height  $h = 220 \text{ nm}$  couples to a gap plasmonic waveguide mode supported by a gold film ( $n = 0.6 + 9.7i$ ) of thickness  $t$  with a gap of width  $g$ . The silicon waveguide is embedded in buried silica oxide ( $n = 1.45$ ), and the region above gold is air ( $n = 1$ ). This structure supports hybrid supermodes  $\beta_i$ , one of which is shown in Fig. 13(a)(ii). The isolated dielectric or plasmonic modes  $\beta_i$  are obtained by either removing the silicon or gold, respectively. For the purpose of illustrating the applicability of our model, we fix all parameters except  $g$  and the device length  $L$ . A fixed  $g$  at the phase matching point along the device length results in a directional coupler, schematically shown in Fig. 13(a)(iii). An adiabatic coupler can be achieved by varying  $g$  across  $L$ , as shown in Fig. 13(a)(iv). We now consider each case separately.

#### 1. Directional coupler

To utilize our directional coupler “explorer’s map”, we first identify the value of  $g$  at which phase matching occurs. The orange dashed lines in Fig. 13(b) show the propagation constant of the lossless isolated plasmonic mode as a function of  $g$ , which intersects the dielectric mode at  $g = 15.8 \text{ nm}$ . The associated lossless coupled modes for a separation  $s = 200 \text{ nm}$  are shown as solid lines. We calculate  $\kappa(z)$  from (24), and plot it as a black line in Fig. 13(d). Finally, we consider the real and imaginary parts of the complex isolated lossy mode effective index, shown as dash-dotted lines in Figs. 13(b) and 13(c), respectively.

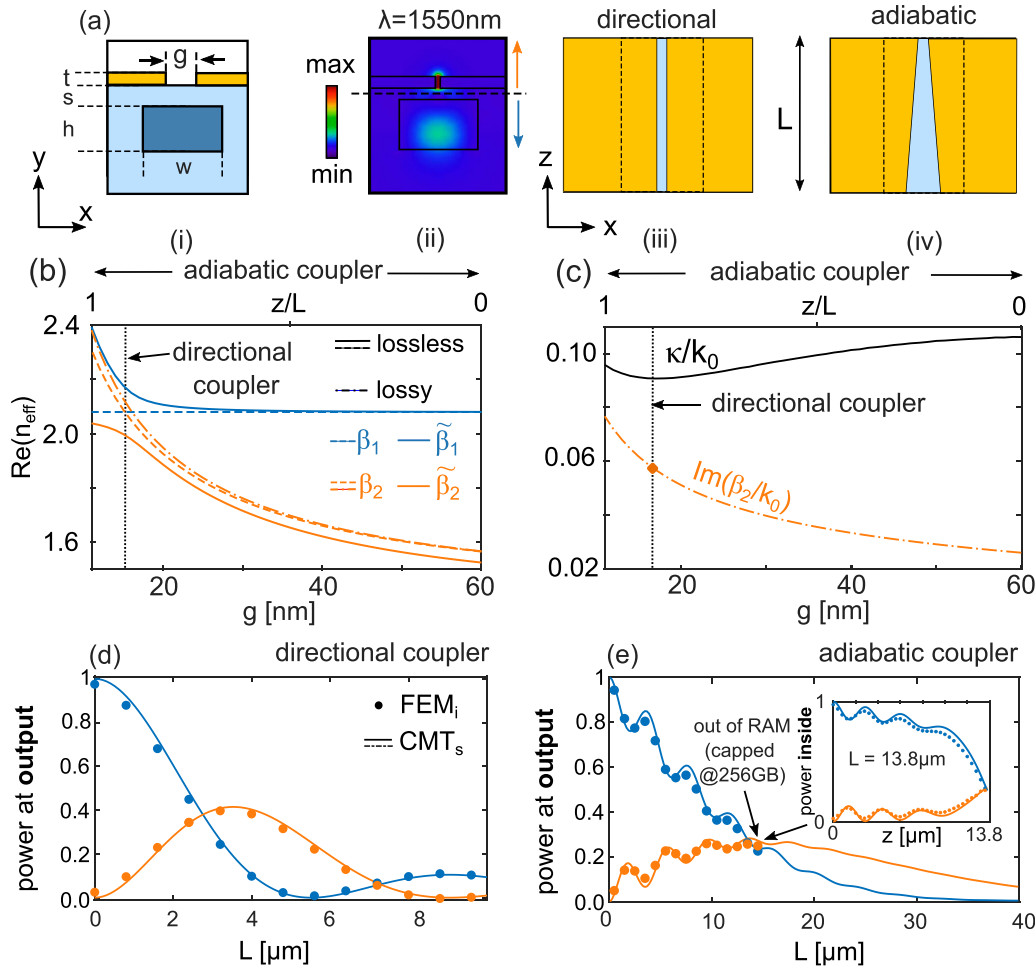


**FIG. 13.** (a) Summary of the chip-scale geometries considered. (i) Cross section: a silicon waveguide (height:  $h = 220$  nm; width:  $w = 350$  nm) buried in a silicon substrate is coated with two metal nanofilms forming a plasmonic slot waveguide with gap width  $g$  on top of the waveguide with edge-to-edge separation  $s$ . (ii) Example supermode profile colormap, showing hybridization between gap plasmon mode and dielectric mode. Top view shows (iii) a directional coupler of length  $L$  where all geometric parameters remain constant, and (iv) an adiabatic coupler, where we take  $g$  to be the only varying parameter. Vertical dashed lines in (iii) and (iv) represent the boundary of the silicon waveguide. (b) Real part of the effective index for  $s = 200$  nm vs the gap width  $g$  for the lossless supermodes (solid lines) and isolated modes (dashed lines) at  $\lambda = 1550$  nm. The dashed-dotted line shows the lossy isolated plasmonic mode. Mode nomenclature and color for dielectric and plasmonic modes coding is analogous to Fig. 2. Vertical black dotted line highlights  $g = 15.8$  nm where the system is a balanced directional coupler. (c) Associated  $\kappa$  (black line) and imaginary part of the isolated plasmonic mode (orange). (d) Power in each region of the directional coupler and (e) adiabatic coupler at the device output (i.e., at  $z = L$ ) as a function of a device of length  $L$ . Inset shows the power in each waveguide inside the device for  $L = 13.8 \mu\text{m}$  calculated using 3D FEM<sub>i</sub> calculations (circles) and CMT<sub>s</sub> (solid lines).

This calculation results in a  $\Delta\tilde{n}_{\text{eff}} = 0.18$  and  $\Im m(\tilde{n}_{\text{eff}}^{(2)}) = 0.058$  [diamond marker in Fig. 13(c)], which according to Fig. 9 predicts a coupling length  $L_{\text{max}} = 2.2\lambda = 3.53 \mu\text{m}$ , with a maximum coupling efficiency of  $\eta_{\text{max}} = 0.41$ . Figure 13(d) shows the calculated power in each waveguide as a function of  $L$  for the directional coupler, as predicted by the CMT<sub>s</sub> model (solid lines) and by FEM<sub>i</sub> calculations (circles), confirming the prediction.

## 2. Adiabatic coupler

We now consider a 3D adiabatic coupler, wherein the gap width  $g$  decreases linearly across the device length, between 60 and 10 nm along  $z$  for different values of  $L$ , as per the upper  $x$  axis in Figs. 13(b)

and 13(c). We repeat the procedure previously used for waveguides whose profile varies, solving (26) numerically for different physical device lengths  $L$ , using the  $z$ -dependent parameters in Fig. 13. The solid lines in Fig. 13(e) shows the resulting  $|\psi_1(L)|^2$  (blue line) and  $|\psi_2(L)|^2$  (orange line) using CMT<sub>s</sub>, which is once again in good agreement with the FEM<sub>i</sub> calculations (circles). Compared to the directional coupler, these results show that this adiabatic coupler has two significant drawbacks: the peak coupling efficiency is lower, and the device length at which it occurs is longer. This is a consequence of the fact that the adiabaticity requirement (i.e., the need for a long device) is adversely affected by the overall loss for this particular design choice, which warrants a further exploration of the design parameters for further improvement—a task that could readily be tackled using CMT<sub>s</sub>.

The inset of Fig. 13(e), which shows that the power inside the device for a fixed length (here:  $L = 13.8 \mu\text{m}$ ), is also well reproduced by our model. Note that, as a result of the small plasmonic gap and long lengths considered, the 3D simulation runs out of memory for  $L > 14 \mu\text{m}$  long device on a high-performance computer, where memory is capped at 256 GB RAM in accordance with reasonable user capabilities.

### B. Fiber-based plasmonic coupler

To show the flexibility of our CMT<sub>s</sub> approach, we now consider fiber-based plasmonic couplers,<sup>76</sup> frequently used in the context of nanofocussing,<sup>30</sup> e.g., with applications in lens-free high resolution

Raman microscopy.<sup>29</sup> Figure 14(a)(i)–(ii) shows a cross-sectional schematic of the device and supported mode at  $\lambda = 0.8 \mu\text{m}$ : the fundamental mode of a cylindrical dielectric silica waveguide ( $n = 1.45$ ) of radius  $R$  hybridized with a radially polarized short-range surface plasmonic waveguide mode supported by a gold nanowire ( $n = 0.23 + 4.51i$ ) of radius  $r = 100 \text{ nm}$  with edge-to-edge separation  $s = 200 \text{ nm}$ . The silicon waveguide is surrounded by air ( $n = 1$ ). This structure supports hybrid supermodes  $\tilde{\beta}_i$ , one of which is shown in Fig. 14(a)(ii). The isolated dielectric or plasmonic modes  $\beta_i$  are obtained by either removing the silica or gold nanowire, respectively. Once again, we fix all parameters except  $R$  and the device length  $L$ . A fixed  $R$  at the phase matching point along the device length results in a directional coupler, schematically shown in Fig. 14(a)(iii). An adiabatic

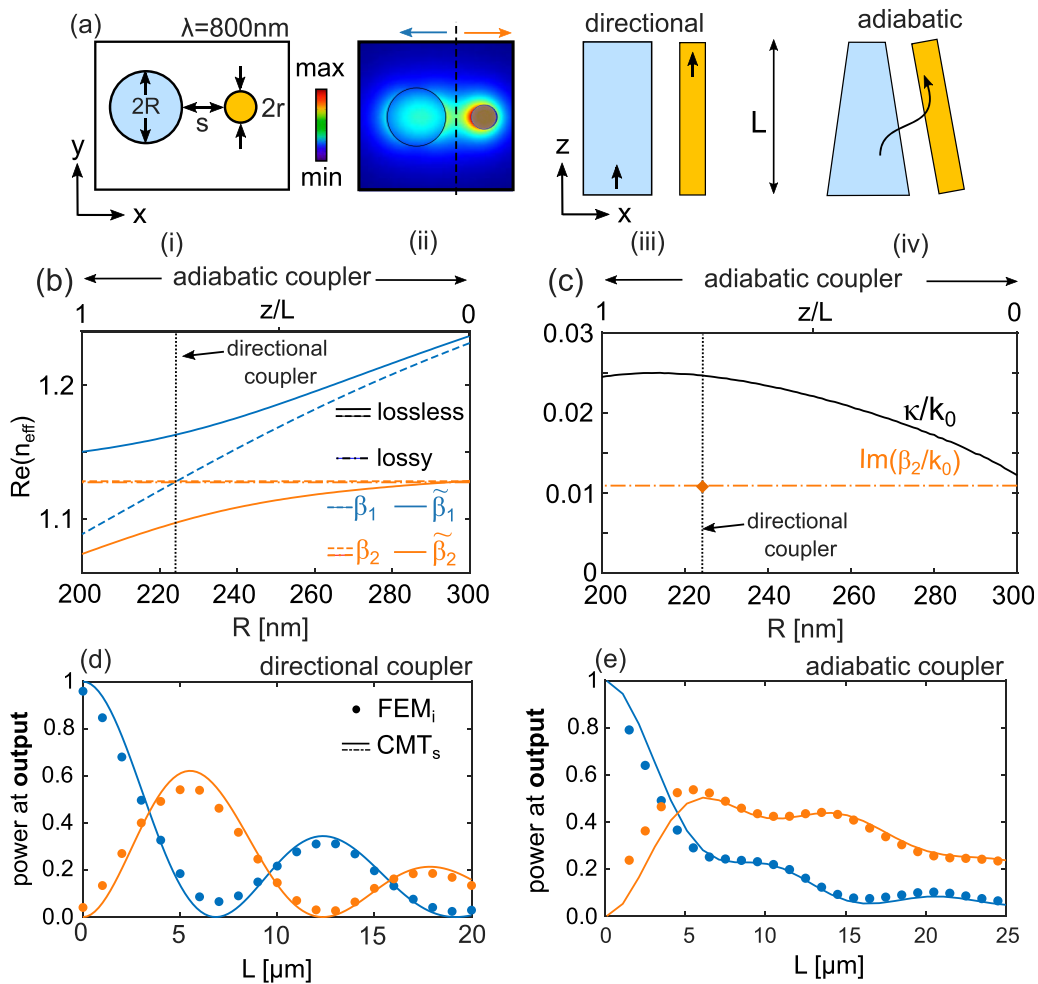


**FIG. 14.** (a) Summary of the fiber-based geometries considered. (i) A cylindrical silica waveguide (radius:  $R$ ) is adjacent to a gold nanowire (radius:  $r = 100 \text{ nm}$ ) in air with edge-to-edge separation  $s = 200 \text{ nm}$ . (ii) Example supermode profile colormap, showing hybridization between radially polarized short-range plasmonic mode and linearly polarized fundamental dielectric waveguide mode. Top view shows (iii) a directional coupler of length  $L$  where all geometric parameters remain constant, and (iv) an adiabatic coupler, where we take  $R$  to be the only varying parameter. (b) Real part of the effective index for  $s = 200 \text{ nm}$  and  $r = 100 \text{ nm}$  as a function of  $R$  for the lossless supermodes (solid lines) and isolated modes (dashed lines) at  $\lambda = 800 \text{ nm}$ . The dash-dotted line shows the lossy isolated plasmonic mode ( $R = 224 \text{ nm}$ ). Mode nomenclature and color for dielectric and plasmonic modes coding is analogous to Fig. 2. Vertical black dotted line highlights  $R = 124 \text{ nm}$  where the device forms a balanced directional coupler. (c) Associated  $\kappa$  (black line) and imaginary part of the isolated plasmonic mode (orange). (d) Power in each region of the directional coupler and (e) adiabatic coupler at the output (i.e., at  $z = L$ ) as a function of a device of length  $L$  calculated using 3D FEM<sub>i</sub> (circles) and CMT<sub>s</sub> (solid lines).

18 April 2024 13:02:07

coupler can be achieved by varying  $R$  across  $L$ , as shown in Fig. 14(a) (iv). In practice, this is achieved by tapering the fiber tip, and placing it next to a gold nanowire, which is a common approach for adiabatic plasmonic focusing.<sup>30</sup>

### 1. Directional coupler

Following our earlier procedure, we identify the value of  $R$  at which phase matching occurs. The orange dashed lines in Fig. 14(b) show the propagation constant of the lossless isolated plasmonic mode as a function of  $R$ , which intersects the dielectric mode at  $R = 224$  nm. The associated lossless coupled modes for a separation  $s = 200$  nm are shown as solid lines. We calculate  $\kappa(z)$  using (24) [black line in Fig. 14(c)] and the real and imaginary parts of the complex isolated lossy modes' effective index [dash-dotted lines in Figs. 14(b) and 14(c)]. This calculation results in a  $\Delta\tilde{n}_{\text{eff}} = 0.066$  and  $\Im m(n_{\text{eff}}^{(2)}) = 0.011$  [diamond marker in Fig. 14(c)], which according to Fig. 9 predicts a coupling length  $L_{\text{max}} = 6.8\lambda = 5.5 \mu\text{m}$ , with a maximum coupling efficiency of  $\eta_{\text{max}} = 0.62$ . Figure 14(d) shows the calculated power in each waveguide as a function of  $L$  for the directional coupler, as predicted by the CMT<sub>s</sub> model (solid lines) and by FEM<sub>i</sub> calculations, showing good agreement with the CMT model.

### 2. Adiabatic coupler

Here, we consider an adiabatic coupler formed by a decreasing dielectric fiber radius  $R$  along the device length, i.e., between 300 and 200 nm along  $z$  for different values of  $L$ , as per the upper x axis in Figs. 14(b) and 14(c). Using these parameters, we repeat the procedure previously used for adiabatic couplers. The solid lines in Fig. 14(e) shows the resulting power in the dielectric (blue line) plasmonic (orange line) regions using CMT<sub>s</sub>, which exhibit good agreement with FEM<sub>i</sub> (circles). In this case, we find a maximum coupling efficiency and minimum device length that is comparable to that of the directional coupler. However, one advantage of this particular adiabatic coupler is that the coupling efficiency is relatively insensitive to the length of the total device, with only small fluctuations in intensity, accompanied by a gradual increase in the overall loss.

## IX. COMPARISON WITH EXPERIMENTS

We now compare CMT<sub>s</sub> directly with plasmonic directional coupler experiments, using published data for the waveguide mode dispersions and transmitted power. Numerous experimental reports of plasmonic directional coupling have been reported.<sup>28,82,83</sup> Here, we analyze the notable and influential work of Degiron *et al.*,<sup>25</sup> whose analysis relied on the eigenmode expansion method using field overlap integrals as per Sec. V "Eigenmode Approaches". We now compare their experiments, summarized in Fig. 5 of Ref. 25 and in Figs. 15(d) and 15(e) with our simplified coupled mode theory where only each modes' effective index is needed.

A schematic of the waveguide cross section considered by Degiron *et al.* is shown in the inset of Fig. 15(a). A SU-8 polymer dielectric waveguide is adjacent to gold nano-strip supporting long-range surface plasmons, both embedded in a layer of benzocyclobutene-based polymer (BCB) on top of a SiO<sub>2</sub> substrate. The gold stripe has a width of  $4.6 \mu\text{m}$  and its thickness is 36 nm, separated from the SU-8 waveguide by a gap of  $2.5 \mu\text{m}$ . In this configuration, the effective indices of the fundamental mode of the dielectric

waveguide and the long-range surface plasmon are adjusted by changing the height of the BCB cladding thickness  $t$ , here obtained by thinning the sample from the top using reactive ion etching. The real and imaginary parts of the effective indices as a function of  $t$  for  $\lambda = 1.55 \mu\text{m}$ , calculated using the finite element method,<sup>25</sup> are shown in Figs. 15(a) and 15(b), respectively. For large values of  $t$ , there is a mode mismatch between the isolated dielectric mode (dark gray line; propagation constant:  $\beta_1$ ) and the plasmonic mode (light gray line; propagation constant:  $\beta_2$ ). For  $t < 10 \mu\text{m}$  the effective indices both drop because much of the field lies in BCB. However, the dielectric waveguide effective index drops more sharply, leading to phase matching when  $t \sim 5.6 \mu\text{m}$ . When the waveguides are placed side by side, the modes hybridize so that the real parts of the supermode eigenvalues anticross, as shown as red and blue curves in Fig. 15(a). The corresponding imaginary parts are shown in Fig. 15(b). Note that all modes' imaginary parts are four orders of magnitude smaller than their real parts, so that they constitute a small perturbation as appropriate for CMT<sub>s</sub>.

In their analysis, Degiron *et al.* used the EM<sub>i</sub> eigenmode method to successfully compare the power in each waveguide as a function of the plasmonic waveguide length. As discussed, this approach relies on overlap integrals between the hybrid and coupled modes, requiring finely meshed field data for each mode involved, which can be resource intensive for large parameter sweeps. We show that the simplified coupled mode theory (CMT<sub>s</sub>) successfully quantitatively reproduces the experiments, by only using the data shown in Figs. 15(a) and 15(b).

As a first step for implementing CMT<sub>s</sub>, we calculate  $\kappa$  via Eq. (24), as a function of  $t$ . Because the imaginary part is small, following our earlier analysis we take  $\Delta = \Re e[(\beta_1 - \beta_2)/2]$  and  $\tilde{\Delta} = \Re e[(\beta_1 - \tilde{\beta}_2)/2]$ , from the data shown in Fig. 15(a). The result is shown in Fig. 15(c), where we find that  $\kappa$  is nominally independent of  $t$ , which is expected given that the positions and dimensions of the gold stripe and the SU-8 waveguide remain unchanged as  $t$  is varied. Furthermore, we find that  $\kappa \ll \beta_{1,2}$ , implying that CMT<sub>s</sub> will provide accurate quantitative predictions as per Fig. 5. Therefore, we obtain the power in the dielectric and plasmonic waveguide, by computing  $\psi_1(z)$  and  $\psi_2(z)$  from Eqs. (30) and (31), respectively, using the complex  $\beta_i$  shown in Figs. 15(a) and 15(b) and the real  $\kappa$  shown in Fig. 15(c).  $|\psi_1|^2$  and  $|\psi_2|^2$  yield the power in each waveguide as a function of device length, which are shown as red and black dash-dotted lines in Figs. 15(d) and 15(e) for  $t = 6.6 \mu\text{m}$  and  $t = 5.4 \mu\text{m}$ , respectively.

In the experiment, the authors couple light ( $\lambda = 1.55 \mu\text{m}$ ) to several dielectric waveguides, each of which is adjacent to a gold strip waveguide of varying length. By measuring the output field profile for each strip length, and integrating the intensity in dielectric and plasmonic regions, the authors retrieve the power transfer properties of the directional coupler, which can be directly compared with our calculations. The inset of Fig. 15(d) shows a typical experimental measurement, showing a double spot intensity pattern due to the field in both the plasmonic and dielectric waveguide regions. The red and black circles in Fig. 15(d) show the associated normalized power emerging from plasmonic and dielectric waveguides, respectively, for  $t = 6.6 \mu\text{m}$ . Figure 15(e) shows the same results for  $t = 5.4 \mu\text{m}$ . The agreement with CMT<sub>s</sub> is excellent. In each case, a periodic exchange of energy occurs between waveguides, which is incomplete due to losses and the fact that in both cases phase matching is not achieved. Note that the CMT<sub>s</sub> model captures the nominal coupling efficiency to the plasmonic mode, which is slightly higher when compared to the phase

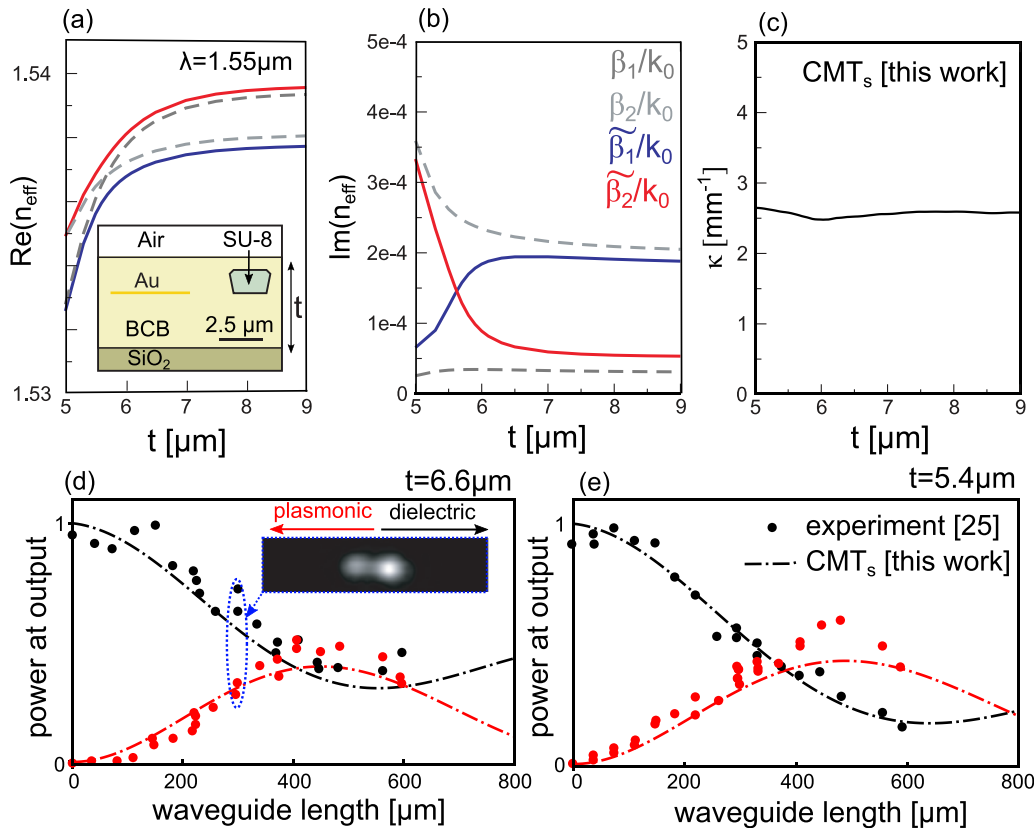


**FIG. 15.** Comparison of plasmonic directional coupler experiments for the geometry presented in Ref. 25 with our calculations using the  $CMT_s$  presented here. A cross section of the waveguide system is shown in the inset of (a). Also shown is the real part of the effective index for the long-range surface plasmon of the isolated gold stripe (light grey), the guided mode of the isolated SU-8 waveguide (dark grey), the symmetric coupled eigenmode (red), and the antisymmetric eigenmode (blue), as a function of CBC thickness  $t$ , for  $\lambda = 1.55 \mu\text{m}$ . (b) Associated imaginary part of the effective index. (c)  $\kappa$  obtained from Eq. (24), using the values plotted in (a) and neglecting loss. (d) Measured intensity transmitted by the dielectric waveguide (black circles) and the Au stripe (red circles) as a function of the waveguide length for a CBC thickness of  $t = 6.6 \mu\text{m}$  and (e)  $t = 5.4 \mu\text{m}$ , in good agreement with  $CMT_s$  (dash-dotted lines). Inset in (d) shows the intensity pattern emitted by the directional coupler for a waveguide length of  $296 \mu\text{m}$  (blue circle), and associated integration regions for obtaining the power in the plasmonic and dielectric regions (red and black, respectively), to left and right of the vertical dashed line. Adapted with permission from A. Degiron *et al.*, *New Journal of Physics* 11, 015002 (2009).<sup>25</sup> Copyright 2009 The Deutsche Physikalische Gesellschaft. Reproduced from IOP Publishing. CC BY-NC-SA, <https://creativecommons.org/licenses/by-nc-sa/3.0/>.

matching point at  $t = 5.4 \mu\text{m}$ . Due to metallic losses however, how well the waveguides couple is best inferred from the extinction in the dielectric waveguide, which goes down at the half beat length when the coupler arms approach the phase matching condition—a feature that is also captured by the simplified theory. This analysis confirms the quantitative appropriateness of  $CMT_s$  for designing realistic three-dimensional devices.

## X. COMPUTATIONAL RESOURCE COMPARISON

To highlight the value and advantages of the simplified coupled mode theory with respect to other methods, which all rely on a wavelength-by-wavelength calculation for a fixed device length, we now discuss and compare the nominal resources necessary for the key calculations presented in this paper, which we performed using a 32 Core 2.4 GHz processor and 256 GB RAM.

Table II(a) shows the typical calculation time and maximum RAM utilized when calculating the power in the plasmonic and dielectric waveguide shown in Fig. 7, i.e., considering 1D modes propagating

in 2D with uniform waveguides. In this case,  $CMT_s$  relies on just propagation constants, which for 1D modes require only 0.05 s per mode and less than 1MB of RAM, using modified publicly available code<sup>84,85</sup> and a single processor core. See Ref. 84 and Ref. 85 for code and information on EM method and  $CMT_s$  method, respectively. The power in each waveguide is then given by Eqs. (30) and (31). Both  $CMT_s$  and EM approaches require, in addition, that fields and overlap integrals be calculated, which increases the time and computational resources by approximately an order of magnitude due to the fine 1D mesh required by the gold nanofilm. By contrast, the finite 2D element methods typically needs several minutes and 11 GB of RAM to complete a single calculation, even for this simple device and when using all 32 processor cores. Clearly,  $CMT_s$  and FEM methods are, respectively, the least and most resource intensive.  $CMT_e$  and EM approaches which use “exact” mode information in the lossy case are less demanding than FEM, but still require the use of cumbersome overlap integrals and vector fields. Their computational cost will always lie somewhere in between  $CMT_s$  and FEM, and increases

**TABLE II.** Summary of the computational resources (time and RAM) for performing the calculations presented here.

(a) 2D Directional Coupler, Fig. 7(d)					
Method	Mode (1D)	Propagation (2D)	Total time	Max. RAM	Comments
CMT <sub>s</sub>	0.01 s	Negligible	0.05 s	<1MB	5 modes No fields needed No overlap integrals
CMT <sub>e</sub> or EM <sub>p,i</sub>	0.2 s	0.02 s	0.6 s	10 MB	3 modes Fields needed 1D mesh: 50k pts. 2D mesh: 300k
FEM (COMSOL)	N.A.	85 s	85 s	11 GB	
(b) 2D Adiabatic Coupler, Fig. 12(e)					
Method	Mode (1D)	Propagation (2D)	Total time	Max. RAM	Comments
CMT <sub>s</sub>	0.01 s (average)	0.1 s (average)	10 s	<1MB	100 calcs., Fig. 12(b) 50 calcs., Fig. 12(e)
FEM (COMSOL)	N.A.	160 s (average)	4000 s	11 GB	25 calcs., Fig. 12(e) 2D mesh: 380k
(c) 3D Directional Coupler, Fig. 13(d)					
Method	Mode (2D)	Propagation (3D)	Total time	Max. RAM	Comments
CMT <sub>s</sub>	5s	Negligible	25 s	300 MB	2D mesh: 11k
FEM (COMSOL)	N.A.	1000 s	1000 s	110 GB	3D mesh: 500k
(d) 3D Adiabatic Coupler, Fig. 13(e)					
Method	Mode (2D)	Propagation (3D)	Total time	Max. RAM	Comments
CMT <sub>s</sub>	5 s (average)	1 s (average)	1650 s	300 MB	50 calcs., Fig. 13(b); 400 calcs., Fig. 13(e); 2D mesh: 11k
FEM (COMSOL)	N.A.	1500 s	22 500 s	256 GB (capped)	15 calcs., Fig. 13(e); 3D mesh: 3M

significantly when propagating in 3D, particularly when fine meshes are required or the device profile varies upon propagation.

Table II(b) shows the resources needed for the CMT<sub>s</sub> and FEM calculations for the 2D adiabatic coupler of Fig. 12. In this case, CMT<sub>s</sub> requires calculating the propagation constants as a function of  $z$  as per Fig. 12(b), and Eq. (26) needs to be integrated numerically using a complex partial differential equation solver (e.g., `scipy` in python, or `ode45` in MATLAB), slightly increasing the overall computational cost relative to the directional coupler.

Finally, Table II(c) and II(d) show the 3D directional and adiabatic coupler calculations shown in Figs. 13(d) and 13(e), respectively. Inevitably, CMT<sub>s</sub> requires the use of 2D mode solvers to obtain the propagation constants, which increases the resources needed. Note, however, that the overall time per mode calculation is still only 5 s, using 300MB of RAM. Full 3D calculations, however, require up to several hundred GB of RAM, and many hours to complete, making CMT<sub>s</sub> particularly advantageous in these scenarios.

Overall, the simplified coupled mode theory method therefore requires resources which are several orders of magnitude less than the

finite element method, and at least one order of magnitude less than eigenmode or other exact methods requiring cumbersome overlap integrals, with the added bonus of providing an essential description of the underlying physics.

## XI. CONCLUSION

In conclusion, we have presented a simplified CMT technique for the rapid and intuitive modeling of compact plasmonic couplers, elucidating where it is quantitatively accurate, and where full methods are required. Although we have presented a two-mode device, we expect that the underlying methodology to be straightforwardly extended when more modes are supported. This method is most suitable at the earliest possible design stage: when starting from scratch, our approach can provide users with estimates of the nominal device length needed, and its associated plasmonic coupling efficiency, using easy-to-calculate mode parameters before embarking on more detailed designs. One particularly important aspect is that the CMT<sub>s</sub> model accurately predicts the coupling length at which the maximum power occurs, although it overestimates the coupling efficiency itself. Although we

have primarily focused on 2D waveguides for ease of comparison with full simulations, the advantages of our method are even more pronounced in otherwise resource-intensive 3D geometries. Our method is well suited to a wide variety of unidirectional coupler structures, whose power distribution can be obtained from closed form equations containing mode parameters that can be immediately calculated. The associated complex propagation constants contain all the information needed to gain first insights into the basic functioning of photonic integrated circuits with plasmonic elements,<sup>86</sup> which will help designers understand the underlying physical mechanisms and provide pathways to optimizing and refining a plasmonic coupler component, e.g., in the context of deep neural networks<sup>76</sup> and inverse design.<sup>87</sup>

## ACKNOWLEDGMENTS

A.T. acknowledges funding from an Australian Research Council Discovery Early Career Researcher Award (DE200101041). A.T. and G.D.V. thank Sabrina Garattoni for fruitful discussions in the early stages of this work.

## AUTHOR DECLARATIONS

### Conflict of Interest

The authors have no conflicts to disclose.

## Author Contributions

**Alessandro Tuniz:** Conceptualization (equal); Data curation (equal); Formal analysis (equal); Funding acquisition (equal); Investigation (equal); Methodology (equal); Project administration (equal); Resources (equal); Software (equal); Supervision (equal); Validation (equal); Visualization (equal); Writing – original draft (equal); Writing – review & editing (equal). **Alex Y. Song:** Formal analysis (supporting); Methodology (supporting); Writing – original draft (supporting); Writing – review & editing (supporting). **Giuseppe Della Valle:** Conceptualization (equal); Formal analysis (supporting); Investigation (supporting); Methodology (supporting); Supervision (supporting); Writing – original draft (supporting); Writing – review & editing (equal). **C. Martijn de Sterke:** Conceptualization (equal); Formal analysis (equal); Investigation (supporting); Methodology (supporting); Supervision (supporting); Writing – original draft (supporting); Writing – review & editing (equal).

## DATA AVAILABILITY

The data that support the findings of this study are available from the corresponding author upon reasonable request.

## REFERENCES

- C. R. Doerr, "Silicon photonic integration in telecommunications," *Front. Phys.* **3**, 37 (2015).
- A. W. Elshari, W. Pernice, K. Srinivasan, O. Benson, and V. Zwiller, "Hybrid integrated quantum photonic circuits," *Nat. Photonics* **14**, 285–298 (2020).
- W. Bogaerts, D. Pérez, J. Capmany, D. A. B. Miller, J. Poon, D. Englund, F. Morichetti, and A. Melloni, "Programmable photonic circuits," *Nature* **586**, 207–216 (2020).
- X. Xu, G. Ren, T. Feleppa, X. Liu, A. Boes, A. Mitchell, and A. J. Lowery, "Self-calibrating programmable photonic integrated circuits," *Nat. Photonics* **16**, 595–602 (2022).
- A. Hänsel and M. J. R. Heck, "Opportunities for photonic integrated circuits in optical gas sensors," *J. Phys.: Photonics* **2**, 012002 (2020).
- W. Bogaerts and L. Chrostowski, "Silicon photonics circuit design: Methods, tools and challenges," *Laser Photonics Rev.* **12**, 1700237 (2018).
- A. Boes, B. Corcoran, L. Chang, J. Bowers, and A. Mitchell, "Status and potential of lithium niobate on insulator (LNOI) for photonic integrated circuits," *Laser Photonics Rev.* **12**, 1700256 (2018).
- M. Merklein, I. V. Kabakova, T. F. S. Büttner, D.-Y. Choi, B. Luther-Davies, S. J. Madden, and B. J. Eggleton, "Enhancing and inhibiting stimulated Brillouin scattering in photonic integrated circuits," *Nat. Commun.* **6**, 6396 (2015).
- A. Rahim, E. Ryckeboer, A. Z. Subramanian, S. Clemmen, B. Kuyken, A. Dhakal, A. Raza, A. Hermans, M. Muneeb, S. Dhoore *et al.*, "Expanding the silicon photonics portfolio with silicon nitride photonic integrated circuits," *J. Lightwave Technol.* **35**, 639–649 (2017).
- R. T. Chen, "Polymer-based photonic integrated circuits," *Opt. Laser Technol.* **25**, 347–365 (1993).
- P. Wen, P. Tiwari, S. Mauthe, H. Schmid, M. Sousa, M. Scherrer, M. Baumann, B. I. Bitachon, J. Leuthold, B. Gotsmann *et al.*, "Waveguide coupled III-V photodiodes monolithically integrated on Si," *Nat. Commun.* **13**, 909 (2022).
- P. Kaur, A. Boes, G. Ren, T. G. Nguyen, G. Roelkens, and A. Mitchell, "Hybrid and heterogeneous photonic integration," *APL Photonics* **6**, 061102 (2021).
- S. A. Maier, *Plasmonics: Fundamentals and applications* (Springer Science & Business Media, 2007).
- L. Novotny and B. Hecht, *Principles of nano-optics* (Cambridge University Press, Cambridge, 2012).
- Y. Meng, Y. Chen, L. Lu, Y. Ding, A. Cusano, J. A. Fan, Q. Hu, K. Wang, Z. Xie, Z. Liu *et al.*, "Optical meta-waveguides for integrated photonics and beyond," *Light: Sci. Appl.* **10**, 235 (2021).
- See <https://www.polariton.ch/> for "Polariton website" (last accessed September 27, 2023).
- A. Tuniz, "Nanoscale nonlinear plasmonics in photonic waveguides and circuits," *La Rivista del Nuovo Cimento* **44**, 193–249 (2021).
- U. Koch, C. Uhl, H. Hettrich, Y. Fedoryshyn, C. Hoessbacher, W. Heni, B. Baeuerle, B. I. Bitachon, A. Josten, M. Ayata *et al.*, "A monolithic bipolar CMOS electronic-plasmonic high-speed transmitter," *Nat. Electron.* **3**, 338–345 (2020).
- K. S. Kunz and R. J. Luebbers, *The Finite Difference Time Domain Method for Electromagnetics* (CRC Press, 1993).
- D. F. G. Gallagher and T. P. Felici, "Eigenmode expansion methods for simulation of optical propagation in photonics: Pros and cons," in *Integrated Optics: Devices, Materials, and Technologies VII* (SPIE, 2003), Vol. 4987, pp. 69–82.
- J.-M. Jin, *The Finite Element Method in Electromagnetics* (John Wiley & Sons, 2015).
- W. Huang, C. Xu, S.-T. Chu, and S. K. Chaudhuri, "The finite-difference vector beam propagation method: Analysis and assessment," *J. Lightwave Technol.* **10**, 295–305 (1992).
- H. A. Haus and W. Huang, "Coupled-mode theory," *Proc. IEEE* **79**, 1505–1518 (1991).
- A. Tuniz, A. Y. Song, G. Della Valle, and C. M. de Sterke, "Plasmonic sensors beyond the phase matching condition: A simplified approach," *Sensors* **22**, 9994 (2022).
- A. Degiron, S.-Y. Cho, T. Tyler, N. M. Jokerst, and D. R. Smith, "Directional coupling between dielectric and long-range plasmon waveguides," *New J. Phys.* **11**, 015002 (2009).
- B. Wild, L. Cao, Y. Sun, B. P. Khanal, E. R. Zubarev, S. K. Gray, N. F. Scherer, and M. Pelton, "Propagation lengths and group velocities of plasmons in chemically synthesized gold and silver nanowires," *ACS Nano* **6**, 472–482 (2012).
- M. P. Nielsen, X. Shi, P. Dichtl, S. A. Maier, and R. F. Oulton, "Giant nonlinear response at a plasmonic nanofocus drives efficient four-wave mixing," *Science* **358**, 1179–1181 (2017).
- F. Lou, Z. Wang, D. Dai, L. Thylen, and L. Wosinski, "Experimental demonstration of ultra-compact directional couplers based on silicon hybrid plasmonic waveguides," *Appl. Phys. Lett.* **100**, 241105 (2012).
- S. Kim, N. Yu, X. Ma, Y. Zhu, Q. Liu, M. Liu, and R. Yan, "High external-efficiency nanofocusing for lens-free near-field optical nanoscopy," *Nat. Photonics* **13**, 636–643 (2019).
- A. Tuniz and M. A. Schmidt, "Interfacing optical fibers with plasmonic nano-concentrators," *Nanophotonics* **7**, 1279–1298 (2018).
- H. Haus, *Waves and Fields in Optoelectronics* (Prentice-Hall, 1984).

- <sup>32</sup>W. Suh, Z. Wang, and S. Fan, "Temporal coupled-mode theory and the presence of non-orthogonal modes in lossless multimode cavities," *IEEE J. Quantum Electron.* **40**, 1511–1518 (2004).
- <sup>33</sup>J. R. Pierce, "Coupling of modes of propagation," *J. Appl. Phys.* **25**, 179–183 (1954).
- <sup>34</sup>S. E. Miller, "Coupled wave theory and waveguide applications," *Bell Syst. Tech. J.* **33**, 661–719 (1954).
- <sup>35</sup>D. Marcuse, "The coupling of degenerate modes in two parallel dielectric waveguides," *Bell Syst. Tech. J.* **50**, 1791–1816 (1971).
- <sup>36</sup>A. W. Snyder, "Coupling of modes on a tapered dielectric cylinder," *IEEE Trans. Microwave Theory Tech.* **18**, 383–392 (1970).
- <sup>37</sup>A. Yariv, "Coupled-mode theory for guided-wave optics," *IEEE J. Quantum Electron.* **9**, 919–933 (1973).
- <sup>38</sup>H. Kogelnik, "Coupled wave theory for thick hologram gratings," *Bell Syst. Tech. J.* **48**, 2909–2947 (1969).
- <sup>39</sup>S. Schelkunoff, "Conversion of Maxwell's equations into generalized telegraphist's equations," *Bell Syst. Tech. J.* **34**, 995–1043 (1955).
- <sup>40</sup>K.-L. Chen and S. Wang, "Cross-talk problems in optical directional couplers," *Appl. Phys. Lett.* **44**, 166–168 (1984).
- <sup>41</sup>H. A. Haus and N. A. Whitaker, Jr., "Elimination of cross talk in optical directional couplers," *Appl. Phys. Lett.* **46**, 1–3 (1985).
- <sup>42</sup>A. Hardy and W. Streifer, "Coupled mode theory of parallel waveguides," *J. Lightwave Technol.* **3**, 1135–1146 (1985).
- <sup>43</sup>H. A. Haus, W. Huang, S. Kawakami, and N. Whitaker, "Coupled-mode theory of optical waveguides," *J. Lightwave Technol.* **5**, 16–23 (1987).
- <sup>44</sup>H. A. Haus, W.-P. Huang, and A. W. Snyder, "Coupled-mode formulations," *Opt. Lett.* **14**, 1222–1224 (1989).
- <sup>45</sup>S.-L. Chuang, "A coupled mode formulation by reciprocity and a variational principle," *J. Lightwave Technol.* **5**, 5–15 (1987).
- <sup>46</sup>W.-P. Huang, "Coupled-mode theory for optical waveguides: An overview," *J. Opt. Soc. Am. A* **11**, 963–983 (1994).
- <sup>47</sup>H. F. Taylor and A. Yariv, "Guided wave optics," *Proc. IEEE* **62**, 1044–1060 (1974).
- <sup>48</sup>H. Kogelnik, "Theory of dielectric waveguides," in *Integrated Optics* (Springer, 1975), pp. 13–81.
- <sup>49</sup>A. W. Snyder, J. D. Love *et al.*, *Optical Waveguide Theory* (Chapman and Hall London, 1983), Vol. 175.
- <sup>50</sup>D. Marcuse, *Theory of Dielectric Optical Waveguides* (Academic Press, 1991).
- <sup>51</sup>S. G. Johnson, M. Ibanescu, M. Skorobogatiy, O. Weisberg, J. Joannopoulos, and Y. Fink, "Perturbation theory for Maxwell's equations with shifting material boundaries," *Phys. Rev. E* **65**, 066611 (2002).
- <sup>52</sup>A. D. Rakić, A. B. Djurišić, J. M. Elazar, and M. L. Majewski, "Optical properties of metallic films for vertical-cavity optoelectronic devices," *Appl. Opt.* **37**, 5271–5283 (1998).
- <sup>53</sup>I. H. Malitson, "Interspecimen comparison of the refractive index of fused silica," *J. Opt. Soc. Am. B* **55**, 1205–1209 (1965).
- <sup>54</sup>A. K. Taras, A. Tuniz, M. A. Bajwa, V. Ng, J. M. Dawes, C. G. Poulton, and C. M. de Sterke, "Shortcuts to adiabaticity in waveguide couplers—theory and implementation," *Adv. Phys.: X* **6**, 1894978 (2021).
- <sup>55</sup>J. Burke, G. Stegeman, and T. Tamer, "Surface-polariton-like waves guided by thin, lossy metal films," *Phys. Rev. B* **33**, 5186 (1986).
- <sup>56</sup>J. Xu and Y. Chen, "General coupled mode theory in non-Hermitian waveguides," *Opt. Express* **23**, 22619–22627 (2015).
- <sup>57</sup>A. Tuniz, M. A. Schmidt, and B. T. Kuhlmeiy, "Influence of non-Hermitian mode topology on refractive index sensing with plasmonic waveguides," *Photonics Res.* **10**, 719–730 (2022).
- <sup>58</sup>A. Tuniz, T. Wieduwilt, and M. A. Schmidt, "Tuning the effective PT phase of plasmonic eigenmodes," *Phys. Rev. Lett.* **123**, 213903 (2019).
- <sup>59</sup>A. Tuniz and M. A. Schmidt, "Broadband efficient directional coupling to short-range plasmons: Towards hybrid fiber nanotips," *Opt. Express* **24**, 7507–7524 (2016).
- <sup>60</sup>A. W. Snyder and J. Love, *Optical Waveguide Theory* (Springer Science & Business Media, 2012).
- <sup>61</sup>X. Sun, H.-C. Liu, and A. Yariv, "Adiabaticity criterion and the shortest adiabatic mode transformer in a coupled-waveguide system," *Opt. Lett.* **34**, 280–282 (2009).
- <sup>62</sup>M. Palamaru and P. Lalanne, "Photonic crystal waveguides: Out-of-plane losses and adiabatic modal conversion," *Appl. Phys. Lett.* **78**, 1466–1468 (2001).
- <sup>63</sup>COMSOL, *Wave Optics Module User's Guide, COMSOL Multiphysics v. 5.3* (COMSOL AB, Stockholm, Sweden, 2017), pp. 47–48.
- <sup>64</sup>V. Ng, A. Tuniz, J. M. Dawes, and C. M. de Sterke, "Insights from a systematic study of crosstalk in adiabatic couplers," *OSA Continuum* **2**, 629–639 (2019).
- <sup>65</sup>T. Chung, S.-Y. Lee, E. Y. Song, H. Chun, and B. Lee, "Plasmonic nanostructures for nano-scale bio-sensing," *Sensors* **11**, 10907–10929 (2011).
- <sup>66</sup>E. Kretschmann and H. Raether, "Radiative decay of non radiative surface plasmons excited by light," *Z. Naturforsch. A* **23**, 2135–2136 (1968).
- <sup>67</sup>A. Otto, "Excitation of nonradiative surface plasma waves in silver by the method of frustrated total reflection," *Z. Phys. A Hadrons Nuclei* **216**, 398–410 (1968).
- <sup>68</sup>F. Peyskens, A. Dhakal, P. Van Dorpe, N. Le Thomas, and R. Baets, "Surface enhanced Raman spectroscopy using a single mode nanophotonic-plasmonic platform," *ACS Photonics* **3**, 102–108 (2016).
- <sup>69</sup>C. Caucheteur, T. Guo, and J. Albert, "Review of plasmonic fiber optic biochemical sensors: Improving the limit of detection," *Anal. Bioanal. Chem.* **407**, 3883–3897 (2015).
- <sup>70</sup>E. Klantsataya, P. Jia, H. Eberdorff-Heidepriem, T. M. Monro, and A. François, "Plasmonic fiber optic refractometric sensors: From conventional architectures to recent design trends," *Sensors* **17**, 12 (2017).
- <sup>71</sup>Y. Xu, P. Bai, X. Zhou, Y. Akimov, C. E. Png, L.-K. Ang, W. Knoll, and L. Wu, "Optical refractive index sensors with plasmonic and photonic structures: Promising and inconvenient truth," *Adv. Opt. Mater.* **7**, 1801433 (2019).
- <sup>72</sup>M.-A. Miri and A. Alù, "Exceptional points in optics and photonics," *Science* **363**, eaar7709 (2019).
- <sup>73</sup>W. Louisell, "Analysis of the single tapered mode coupler," *Bell Syst. Tech. J.* **34**, 853–870 (1955).
- <sup>74</sup>D. Guéry-Odelin, A. Ruschhaupt, A. Kiely, E. Torrontegui, S. Martínez-Garaot, and J. G. Muga, "Shortcuts to adiabaticity: Concepts, methods, and applications," *Rev. Mod. Phys.* **91**, 045001 (2019).
- <sup>75</sup>M. I. Stockman, "Nanofocusing of optical energy in tapered plasmonic waveguides," *Phys. Rev. Lett.* **93**, 137404 (2004).
- <sup>76</sup>B. Liang, D. Xu, N. Yu, Y. Xu, X. Ma, Q. Liu, M. S. Asif, R. Yan, and M. Liu, "Physics-guided neural-network-based inverse design of a photonic-plasmonic nanodevice for superfocusing," *ACS Appl. Mater. Interfaces* **14**, 27397–27404 (2022).
- <sup>77</sup>Q. Li and M. Qiu, "Structurally-tolerant vertical directional coupling between metal-insulator-metal plasmonic waveguide and silicon dielectric waveguide," *Opt. Express* **18**, 15531–15543 (2010).
- <sup>78</sup>C. Delacour, S. Blaize, P. Grosse, J. M. Fedeli, A. Bruyant, R. Salas-Montiel, G. Lerondel, and A. Chelnokov, "Efficient directional coupling between silicon and copper plasmonic nanoslot waveguides: Toward metal-oxide-silicon nanophotonics," *Nano Lett.* **10**, 2922–2926 (2010).
- <sup>79</sup>G. Dabos, D. Ketzaki, A. Manolis, E. Chatzianagnostou, L. Markey, J.-C. Weeber, A. Dereux, A. L. Giesecke, C. Porschatis, B. Chmielak *et al.*, "Water cladded plasmonic slot waveguide vertically coupled with si 3 n 4 photonics," *IEEE Photonics J.* **10**, 2700308 (2018).
- <sup>80</sup>S. Eslami and S. Palomba, "Integrated enhanced Raman scattering: A review," *Nano Convergence* **8**, 41 (2021).
- <sup>81</sup>M. Fu, M. P. d P. Mota, X. Xiao, A. Jacassi, N. A. Günsken, Y. Chen, H. Xiao, Y. Li, A. Riaz, S. A. Maier *et al.*, "Near-unity Raman  $\beta$ -factor of surface-enhanced Raman scattering in a waveguide," *Nat. Nanotechnol.* **17**, 1251–1257 (2022).
- <sup>82</sup>T. Holmgaard, Z. Chen, S. I. Bozhevolnyi, L. Markey, and A. Dereux, "Design and characterization of dielectric-loaded plasmonic directional couplers," *J. Lightwave Technol.* **27**, 5521–5528 (2009).
- <sup>83</sup>F. Liu, Y. Li, R. Wan, Y. Huang, X. Feng, and W. Zhang, "Hybrid coupling between long-range surface plasmon polariton mode and dielectric waveguide mode," *J. Lightwave Technol.* **29**, 1265–1273 (2011).
- <sup>84</sup>See <https://github.com/tuniz/plasmonic-sensor> for code and more information on EM method (last accessed January 16, 2024).
- <sup>85</sup>See <https://github.com/tuniz/sensors> for code and more information on CMTs method (last accessed January 16, 2024).
- <sup>86</sup>T. J. Davis, D. E. Gómez, and A. Roberts, "Plasmonic circuits for manipulating optical information," *Nanophotonics* **6**, 543–559 (2016).
- <sup>87</sup>T. Zhang, J. Wang, Q. Liu, J. Zhou, J. Dai, X. Han, Y. Zhou, and K. Xu, "Efficient spectrum prediction and inverse design for plasmonic waveguide systems based on artificial neural networks," *Photonics Res.* **7**, 368–380 (2019).